Computer Physics Communications 317 (2025) 109852

Contents lists available at ScienceDirect

Computer Physics Communications

journal homepage: www.elsevier.com/locate/cpc

Computational Physics

A Lattice Boltzmann method for free surface flows over partially submerged structures

Baoming Guo [a], Jianping Meng [b], Zhihua Xie [a], Dezhi Ning [c], Shunqi Pan [a,*]

[a] Hydro-environmental Research Centre, School of Engineering, Cardiff University, CF24 3AA, UK
[b] Research IT, IT Services, University of Liverpool, L69 3GG UK
[c] State Key Laboratory of Coastal and Offshore Engineering, Dalian University of Technology, Dalian 116024, China

ARTICLE INFO

Edited by Editor: Prof. Andrew Hazel

Keywords:
Lattice Boltzmann method (LBM)
Volume-of-fluid (VOF)
Partially submerged structures
Hydrodynamic forces

ABSTRACT

The Lattice Boltzmann method (LBM) has been extensively developed to efficiently simulate free surface flows and interactions between single-phase flows and fully immersed structures. However, few studies have focused on modelling partially submerged structures, particularly on accurately evaluating their hydrodynamic forces under gravity and wave dynamic conditions. To advance the application of LBM in this area, this study presents a dynamic-pressure Lattice Boltzmann model tailored for simulating partially submerged stationary structures in free surface flows. In the free surface section, the volume-of-fluid method is implemented and the advection of volume fraction is governed by the streaming of intrinsic density distribution functions. For the fluid-structure interface, an interpolated bounce-back scheme is imposed on the no-slip fluid-structure boundary and an improved momentum exchange method is employed to assess the fluid loads, accounting for the effects of gravity and external sources. This paper details the implementation of modelling framework and presents the outcomes of five benchmark simulations conducted for model verification and validation. These cases include flows over a circular cylinder and a square cylinder, Rider-Kothe single vortex evolution, dam-break flows, and wave impact on two partially submerged fixed boxes. The developed numerical model yields satisfactory agreement with experimental and numerical results in terms of the hydrodynamic force evaluation and free surface deformation. The final case demonstrates the capability of the LBM model in investigating frequency response of wave impact on partially submerged structures, highlighting its potential for broader applications in coastal and ocean engineering.

1. Introduction

Marine structures interacted with free surface flows are a common focus in coastal and ocean engineering, involving applications such as wave energy converters (WECs) [1], floating liquid natural gas (FLNG) production systems [2,3], and offshore wind farms platforms [4] interacting with ocean waves and currents. Such a hydrodynamic problem often involves violent deformation of high-density-ratio air-water interface and strong slamming forces impacts on structures. Efficiently simulating the complex free surface fluid-structure interaction still remains a challenging task for computational fluid dynamics (CFD) [5]. With respect to conventional Navier-Stoke (NS) CFD methods, the Lattice Boltzmann method (LBM) offers several attractive features: linear advection between nodes, localized nonlinear fluid dynamics, and independence from solving Poisson equation [6]. These characteristics render LBM particularly well-suited for high-performance computing (HPC) on parallel architectures. With significant advancements on parallel HPC over the last decades, LBM has developed to be an efficient and powerful numerical tool for modelling both free surface flows [7,8] and hydrodynamics of immersed structures [9–11].

For studying an offshore structure coupling with free surface flows, it is essential to address two crucial aspects: gas-liquid interface capturing and fluid-structure boundary treatment. Within LBM, both diffuse interface and sharp interface capturing methods can be applied to model the free surface flows. The diffuse interface capturing method, popular in the early development of LBM for multi-phase flows with low Reynolds numbers, includes various models such as the colour-gradient [12], free-energy [13], and Shan-Chen pseudopotential [14] models. These models are powerful for simulating multiphase flows with complex geometries and topologies. However, for applications involving

---

* Corresponding author.
E-mail address: pans2@cardiff.ac.uk (S. Pan).

https://doi.org/10.1016/j.cpc.2025.109852
Received 5 February 2025; Received in revised form 27 August 2025; Accepted 3 September 2025

high density and viscosity ratios or when computational resources are limited, sharp interface capturing methods might be preferred [8]. In terms of this, the volume-of-fluid (VOF) and level set methods have been incorporated into LBM [15,16]. These LBM-based sharp interface capturing methods solve the same advection equation of volume fraction (for VOF) or signed-distance functions (for level set) similarly to the NS-based methods. Specifically, in the Level Set approach, the algorithm for solving signed distance functions, which is independent from LBM evolutions, is the same as those used in NS-based solvers [16,17]. In the VOF approach, Korner et al [15] initially integrated the VOF method into LBM model where the advection of volume fraction is evaluated by the streaming of intrinsic density distribution functions (DFs), while Janssen and Krafczyk [18] coupled LBM with NS solver's VOF algorithm, employing the piecewise linear interface reconstruction (PLIC). Recently, the VOF-LBM and Level Set-LBM models have been extended to coastal and ocean engineering. For example, the dam-break flows characterized by high Reynolds numbers were modelled in several studies to validate their free surface models [5,17–19], involving interface reconstruction algorithm, GPU implementation, and combination of cumulant LBM. In wave dynamics simulations, Thorimbert et al [20] and Liu et al [21] observed wave energy dissipation and spurious current problems in their numerical wave model based on the original Korner's VOF method, attributed to inconsistencies between gravity and pressure gradients. To address these, Liu et al [22] introduced the gravity into the pressure gradient term to reduce force imbalance-induced errors. Qiu et al [23] combined the VOF-LBM model with a fluid-structure boundary treatment approach for modelling landslide-induced tsunami waves. These studies concentrate on enhancing the free surface algorithms for stably and efficiently capturing the air-water interface deformation. They demonstrate that LBM has been effectively utilized for simulating free surface flows.

In terms of the fluid-structure boundary treatment, the numerical approach in the framework of LBM is broadly categorized into the bounce-back (BB) method, sharp-interface immersed boundary method (IBM), and diffused-interface IBM [6,24]. The BB treatment is intuitive and simple to implement the no-slip boundary conditions and is proven highly accurate and efficient for stationary boundaries with higher-order interpolated methods, while the IBM is advantageous for handling complex moving solid boundary, particularly the flexible deforming structures. Hydrodynamic force evaluations normally depend on the solid boundary treatment scheme. For diffused-interface IBM, the hydrodynamic forces can be evaluated by integrating the boundary forces at Lagrangian solid nodes or at Eulerian fluid nodes. Meanwhile, the stress integration method (SIM) and momentum exchange method (MEM) [25] can be applied to the fluid loads calculation in BB and sharp-interface IBM approaches. The SIM, initially developed in NS solvers, integrates the stress and pressure along the body surface. Although the stress in LBM can be evaluated locally through the second-order velocity moment of non-equilibrium DFs, the extrapolation of DFs from nodes to solid boundary inevitably introduces instability and inefficiency [11,25]. Conversely, the MEM aligns well with the LBM evolution characteristics where the hydrodynamic force acting on structure equals the momentum change of fluid particles after the collision with the solid boundary. The conventional MEM violates local Galilean invariance, limiting its application for moving structures. Chen et al [26] and Wen et al [27] proposed corrections for MEM to restore the local Galilean invariance by taking the structure velocity into consideration, known as Galilean-invariant momentum exchange method (GIMEM). Various benchmark cases have been simulated to validate the numerical approaches for fluid-structure treatment in laminar flows [10,11,28], including freely-settling cylinder in the vertical channel, transient laminar pipe flow, and flapping flag. For turbulent flows with complex geometries, the performance of interpolated BB and IBM have also been tested and compared through turbulent pipe flows and particle-laden flows [29,30]. Practically, Morrison and Leder [9] applied BB approach to study the scour and sedimentation around a horizontally bedded finite cylinder subjected to the uniform water flow. Fringand et al [31] established an IBM-LBM solver to investigate the dynamics of an elastic beam behind a cylinder, immersed in a parabolic turbulent flow. Overall, these fluid-structure treatment approaches in LBM have been well-developed and successfully applied to simulation of structures/solid particles in single-phase flows without an air-water interface.

Regarding the free surface flows over structures in LBM, Zhao et al [32] simulated wave deformation over a submerged breakwater based on depth-integrated continuity equation method and BB approaches. This water scattering by submerged structures was also modelled by others [21,22], using Korner's VOF method combined with the BB approach. For these fully immersed structures, the numerical treatments for the free surface and the fluid-solid boundary are independent, facilitating straightforward integration of fluid-structure treatment approaches into the free surface model. Efforts to extend LBM to partially submerged structures, which require coupled treatments of fluid-structure and free surface boundaries, have also been made. Using the diffuse-interface capturing method, Watanabe et al [33] applied the single-phase conservative phase-field method combining BB approaches to investigate the tsunami flows interacting with floating structures. Zhou et al [34] combined two-phase conservative phase-field approach with a central-moment collision model to construct a numerical wave tank and simulate the shoaling-induced wave deformation and breaking. Based on the sharp-interface VOF method, Janssen and Krafczyk [19], for example, employed the simple bounce back (SBB) scheme [35] in their GPU-based model to evaluate the slamming forces on a land-fixed cylinder subjected to dam-break flows. Sato et al [36] measured the water height and point pressure at a cubic structure surface during dam-break flows. Additionally, Thorimbert et al [20] investigated wave propagating through a fixed oscillating water column WEC, combining the VOF and BB approaches, and Liu et al [7] simulated a wave propagation around square cylinder and circular cone within their dynamic pressure scheme [22]. Since fully three-dimensional VOF simulations demand substantial computational resources, Yuan et al [37] coupled a two-dimensional shallow water model with the VOF-LBM model for modelling flood wave evolution in reservoirs and riverbeds. Most existing studies focus primarily on the influence of stationary structures on free surface deformation, while the reverse effect, the hydrodynamic forces exerted by free surface flows on structures, has received comparatively little attention, despite its critical importance for the safe design and operation of such structures. In particular, the hydrostatic pressure gradient induced by gravity can lead to significant force fluctuations, even when higher-order interpolation schemes are employed at the fluid-structure interface in LBM, as reported by Bogner and Rüde [38]. This highlights the need for improved force evaluation techniques to ensure accurate and robust prediction of hydrodynamic forces.

As reviewed above, previous LBM studies have primarily addressed either fully submerged bodies or free surface dynamics in isolation. Only a limited number of works have attempted to simulate free surface flows around partially submerged structures. Within the diffuse-interface framework, the phase-field-based solver developed by Watanabe et al [33] has demonstrated promising accuracy and robustness for this class of problems. However, the development of corresponding sharp-interface methods in the context of LBM remains relatively immature. This challenge involves the complex boundary treatment required at the triple junction where gas, liquid, and solid phases intersect. Furthermore, the presence of hydrostatic pressure gradients continues to complicate the accurate computation of forces on structures. To address these challenges, this study aims to develop a sharp-interface VOF model combining with BB approaches within dynamic-pressure LB framework for simulating the partially submerged stationary structures in free surface flows and correctly evaluating the hydrodynamic forces. The remaining part of this paper is structured as follows: Section 2 describes the LBM including the multi-relaxation-time model, free surface capturing, and fluid-structure treatment method. The wave generation and absorption technique, and code performance are also incorporated into this section. Section 3 verifies the accuracy of

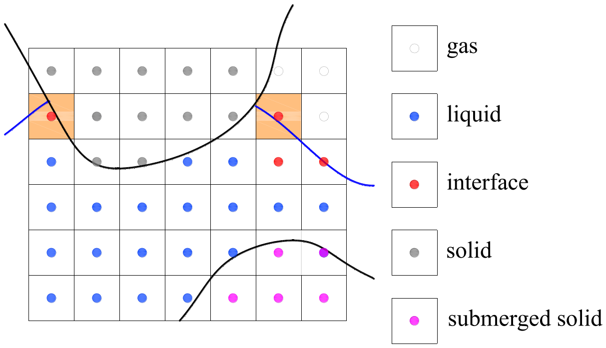

Fig. 1. Schematic diagram for partially submerged structure in free surface flows (the solid blue line is the free surface, and the arrow lines denote that DFs from gas and solid nodes are reconstructed using either the free surface or the bounce-back boundary condition schemes).

the hydrodynamic force evaluation and free surface deformation. Section 4 presents the model validation with two practical cases of fluid flows with high Reynolds number: classic dam-break flows and wave flow past partially submerged structures.

2. Numerical model

In this study, a numerical framework is developed using the Lattice Boltzmann method within the dynamic pressure scheme [22] for simulating partially submerged stationary structures in free surface flows, as shown in Fig. 1, where the partially submerged structure is represented as grey nodes. The VOF method [15], extensively applied in most of the aforementioned studies, is implemented here to capture the free surface. For fluid-stationary structure treatment, the interpolated bounce-back method (IBB) with relatively high accuracy is used at the solid wall boundary with the no-slip condition. The MEM is extended for force evaluation of partially submerged body within the present dynamic pressure LB scheme. The coupling problems of fluid-structure treatment and free surface capture algorithms are addressed.

2.1. *Multi-relaxation-time lattice boltzmann model*

For the isothermal incompressible flows, the governing equation is the continuous Boltzmann equation [6],

$$\frac{\partial f}{\partial t}+\boldsymbol{e}\cdot\frac{\partial f}{\partial \boldsymbol{x}}+\mathscr{F}\cdot\frac{\partial f}{\partial \boldsymbol{e}}=\Omega(f) \tag{1}$$

where $f(\boldsymbol{x},\boldsymbol{e},t)$ is the molecular distribution function at position $\boldsymbol{x}$ and time t for molecular velocity $\boldsymbol{e}$, and $\mathscr{F}$ is the external body force per unit mass. $\Omega(f)$ is the collision operator. Within multi-relaxation-time (MRT) collision model, extending beyond the Bhatnagar-Gross-Krook (BGK) approach [39], it can be rewritten as a discrete equation by fully discretizing in the time t, space $\boldsymbol{x}$ and molecular velocity $\boldsymbol{e}$,

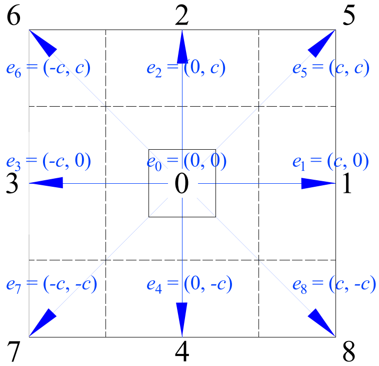

Fig. 2. Discretised directions and molecular velocities in a D2Q9 LBM discretization.

$$f_\alpha(\boldsymbol{x}+\delta\boldsymbol{x}_\alpha,t+\delta t)-f_\alpha(\boldsymbol{x},t)=-\boldsymbol{M}^{-1}[\boldsymbol{S}\cdot(\boldsymbol{m}-\boldsymbol{m}^{\mathrm{eq}})]+\boldsymbol{M}^{-1}\left(\boldsymbol{I}-\frac{1}{2}\boldsymbol{S}\right)\boldsymbol{\Phi}\delta t \tag{2}$$

in which, f_α and $\boldsymbol{e}_\alpha$ are the discretised molecular distribution function and molecular velocity in direction α; $\delta\boldsymbol{x}_\alpha=\boldsymbol{e}_\alpha\delta t$; δt and $\delta x=\sqrt{3}c_s\delta t$ are the time step and space step, respectively, where c_s is the sound speed ($c_s=\sqrt{RT_0}$, where R and T_0 is the specific gas constant and reference temperature [40,41]).

In the present two-dimensional study, the commonly used D2Q9 scheme (nine molecular velocities in two space dimensions) is adopted, as shown in Fig. 2. In the standard MRT-LBM model, the relaxation matrix $\boldsymbol{S}=\mathrm{diag}(1,\ \omega_e,\ \omega_\epsilon,1,\ \omega_q,1,\ \omega_q,\ \omega_\nu,\ \omega_\nu)$, where ω_e and $\omega_\nu=1/(\tau/\delta t+0.5)$ are the bulk and shear viscosities, respectively, and ω_e, ω_ϵ and ω_q can be adjusted for numerical stability and accuracy. τ is the non-dimensional relaxation time. The transformation matrix $\boldsymbol{M}$ to map distributions f_α in the moment space, the equilibrium moments $\boldsymbol{m}^{\mathrm{eq}}=\boldsymbol{M}f^{\mathrm{eq}}$, and force term in the moment space $\boldsymbol{\Phi}=\boldsymbol{M}\mathscr{F}$ with Guo Force scheme [42] for $\mathscr{F}$, can be expressed as,

$$\left\{\boldsymbol{M}_\alpha\quad\frac{\boldsymbol{m}^{\mathrm{eq}}}{\rho}\quad\frac{\boldsymbol{\Phi}}{\rho}\quad\boldsymbol{w}\right\}=\left\{\begin{matrix}1 & 1 & 0 & 4/9\\ \|\boldsymbol{e}_\alpha\|^2-4 & \|\boldsymbol{u}\|^2-2 & 2(\boldsymbol{\mathcal{F}}\cdot\boldsymbol{u}) & 1/9\\ \frac{1}{2}\|\boldsymbol{e}_\alpha\|^4-\frac{7}{2}\|\boldsymbol{e}_\alpha\|^2+4 & 1-\|\boldsymbol{u}\|^2 & -2(\boldsymbol{\mathcal{F}}\cdot\boldsymbol{u}) & 1/9\\ e_{\alpha,x} & u_x & \mathcal{F}_x & 1/9\\ (\|\boldsymbol{e}_\alpha\|^2-5)e_{\alpha,x} & -u_x & -\mathcal{F}_x & 1/9\\ e_{\alpha,y} & u_y & \mathcal{F}_y & 1/36\\ (\|\boldsymbol{e}_\alpha\|^2-5)e_{\alpha,y} & -u_y & -\mathcal{F}_y & 1/36\\ e_{\alpha,x}^2-\ e_{\alpha,y}^2 & u_x^2-u_y^2 & 2\left(\mathcal{F}_yu_x+\mathcal{F}_xu_y\right) & 1/36\\ e_{\alpha,x}e_{\alpha,y} & u_xu_y & \mathcal{F}_yu_x+\mathcal{F}_xu_y & 1/36\end{matrix}\right\} \tag{3}$$

where $\boldsymbol{u}$ is the macroscopic velocity and $\boldsymbol{w}$ is the weight coefficient specific to each molecular velocity discretisation. It should be noted that some revisions for , $\boldsymbol{m}^{\mathrm{eq}}$ and $\boldsymbol{\Phi}$ have been made to adapt the LBM model based on [40,41]. The second-order equilibrium molecular distribution function f_α^{eq} is expressed as,

$$f_\alpha^{\mathrm{eq}}(\boldsymbol{x},t)=w_\alpha\rho\left[1+\frac{\boldsymbol{e}_\alpha\cdot\boldsymbol{u}}{c_s^2}+\frac{(\boldsymbol{e}_\alpha\cdot\boldsymbol{u})^2}{2c_s^4}-\frac{\boldsymbol{u}^2}{2c_s^2}\right] \tag{4}$$

The macroscopic quantities can be calculated by the velocity moments,

$$\rho=\sum_\alpha f_\alpha,\ \boldsymbol{u}=\sum_\alpha \boldsymbol{e}_\alpha f_\alpha\bigg/\rho+\frac{\mathscr{F}}{2}\delta t \tag{5}$$

where α is molecular velocity direction. More details regarding the MRT-LBM model can be found in [6,22,43].

The N-S equations can be recovered through the Chapman-Enskog expansion [6] as,

$$\begin{gathered}\frac{\partial\rho}{\partial t}+\frac{\partial(\rho u_i)}{\partial x_i}=0\\ \frac{\partial(\rho u_i)}{\partial t}+\frac{\partial(\rho u_i u_j)}{\partial x_j}=-\frac{\partial p}{\partial x_i}+\frac{\partial}{\partial x_j}\left(\mu\left(\frac{\partial u_i}{\partial x_j}+\frac{\partial u_j}{\partial x_i}\right)+\left(\mu_{\mathrm{B}}-\frac{2\mu}{3}\right)\delta_{ij}\frac{\partial u_k}{\partial x_k}\right)+\rho\mathscr{F}_i\end{gathered} \tag{6}$$

where $p=\rho c_s^2$, shear viscosity $\mu=p\left(\frac{\delta t}{\omega_\nu}-0.5\delta t\right)$, bulk viscosity $\mu_{\mathrm{B}}=p\left(\frac{\delta t}{\omega_e}-0.5\delta t\right)-\frac{\mu}{3}$ and $\mathscr{F}_i$ is the force terms, including the gravity force and source term from wave generation and absorption methods.

Liu et al [22] demonstrated that the inconsistency of gravity and pressure gradient induces the unphysical current and further causes the numerical instability and energy dissipation. Bogner and Rüde [38] also pointed out that the buoyancy force from the hydrostatic pressure gradient cannot be accurately evaluated due to the staircase approximation of the liquid-solid interface on Cartesian grids. To reduce those numerical errors, the modified-pressure LB scheme developed by Liu et al [22] is applied here. In this scheme, the gravity is incorporated into the pressure gradient term as $p^*=p-\rho_0\boldsymbol{g}(\boldsymbol{x}-\boldsymbol{x}_{\mathrm{ref}})$. The reference surface is chosen as the still water surface.

$$\begin{gathered}\frac{\partial\rho}{\partial t}+\frac{\partial(\rho u_i)}{\partial x_i}=0\\ \frac{\partial\rho u_i}{\partial t}+\frac{\partial(\rho u_i u_j)}{\partial x_j}=-\frac{\partial p^*}{\partial x_i}+\frac{\partial}{\partial x_j}\left(\mu\left(\frac{\partial u_i}{\partial x_j}+\frac{\partial u_j}{\partial x_i}\right)+\left(\mu_{\mathrm{B}}-\frac{2\mu}{3}\right)\delta_{ij}\frac{\partial u_k}{\partial x_k}\right)+\rho(\mathscr{F}_i-g_i)\end{gathered} \tag{7}$$

To include the turbulent effects at some scales for the free surface flows characterized by high Reynolds numbers, a large eddy simulation subgrid-scale model, i.e., the Smagorinsky model, is used as,

$$\begin{gathered}\mu=\mu_{\mathrm{f}}+\mu_{\mathrm{t}}\\ \mu_{\mathrm{t}}=\rho(C_s\delta)^2\|\overline{\boldsymbol{S}}\|=\rho(C_s\delta)^2\frac{\|\overline{\boldsymbol{\sigma}}\|}{2\mu}\end{gathered} \tag{8}$$

where, μ is the total dynamic viscosity; μ_{f} is the fluid dynamic viscosity; μ_{t} is the turbulent eddy viscosity; C_s is the Smagorinsky coefficient, in the range of 0.05–0.18; $\delta=\delta_x$ is the filter length; and $\|\overline{\boldsymbol{\sigma}}\|=\sqrt{2\overline{\sigma}_{ij}\overline{\sigma}_{ij}}$ where $\overline{\sigma}_{ij}$ is stress tensor evaluated by the second-order velocity moment of non-equilibrium part in LBM as,

$$\begin{cases}\overline{S}_{ij}=-\dfrac{\overline{\sigma}_{ij}}{2\mu}=-\dfrac{1}{2p\tau}\dfrac{2\tau}{2\tau+\delta t}\widehat{\sigma}_{ij}\\ \widehat{\sigma}_{ij}=\sum_\alpha e_{\alpha i}e_{\alpha j}\left(f_\alpha-f_\alpha^{\mathrm{eq}}\right)\end{cases} \tag{9}$$

Substituting Eq. (9) into Eq. (8), which yields,

$$\tau=\frac{1}{2}(\tau_{\mathrm{f}}-0.5\delta t)+\frac{1}{2}\sqrt{(\tau_{\mathrm{f}}+0.5\delta t)^2+\frac{2(C_s\delta)^2}{\rho c_s^4}\sqrt{2\widehat{\sigma}_{ij}\widehat{\sigma}_{ij}}} \tag{10}$$

Following [40,41], the non-dimensional variables (with hat) are adopted in this study expressed as:

$$\begin{gathered}\widehat{x}_i=\frac{x_i}{L_0},\ \widehat{u}_i=\frac{u_i}{\sqrt{RT_0}},\widehat{t}=\frac{t}{L_0/\sqrt{RT_0}},\ \widehat{g}_i=\frac{g_i}{RT_0/L_0},\ \widehat{T}=\frac{T}{T_0},\\ \widehat{\tau}=\frac{\tau}{L_0/\sqrt{RT_0}},\ \widehat{p}=\frac{p}{p_0},\ \widehat{\rho}=\frac{\rho}{\rho_0},\ \widehat{\sigma}_{ij}=\frac{\sigma_{ij}}{p_0},\ \widehat{\tau}=\frac{\mu}{\rho_0\sqrt{RT_0}L_0}\end{gathered}$$

For brevity hereafter, the hat symbol is removed from the non-dimensional quantities.

2.2. Free surface capturing method

The single-phase VOF is applied to capture the gas-liquid interface where the volume fraction of liquid ε in each cell is used to determine the cell state: liquid ($\varepsilon=1$), gas ($\varepsilon=0$) or interface ($0<\varepsilon<1$). It is assumed that the dynamics of gas phase is not simulated through LBM, and a free surface boundary condition is imposed at the interface cells to reconstruct the DFs for the balance of hydrodynamic stress and gas pressure, instead. Concerning partially submerged structures, the concept of porosity and solid fraction is introduced to address a situation that a cell is occupied by gas, liquid and solid phases simultaneously, as the cells in orange colour shown in Fig. 1.

$$\varepsilon(\boldsymbol{x},t)=\frac{m(\boldsymbol{x},t)}{\varphi(\boldsymbol{x},t)\delta x^2\rho(\boldsymbol{x},t)} \tag{11}$$

where m and ρ are the mass and density of liquid phase, respectively, $\varphi(\boldsymbol{x},t)=1-\varepsilon_{\mathrm{s}}$ is the porosity and ε_{s} is the solid fraction ($\varepsilon_{\mathrm{s}}=V_{\mathrm{s}}/\delta x^2$). During the streaming, the free surface movement in those interface cells is captured by computing the mass exchange between local $\boldsymbol{x}$ and neighbouring cells $\boldsymbol{x}+\delta\boldsymbol{x}_\alpha$,

$$\frac{\partial\rho}{\partial t}+\nabla\cdot(\rho\boldsymbol{u})=0\rightarrow m(\boldsymbol{x},t+\delta t)=m(\boldsymbol{x},t)+\sum_\alpha\Delta m_\alpha \tag{12}$$

The mass exchange Δm_α, associated with the convective term is evaluated as,

$$\Delta m_\alpha(\boldsymbol{x},t)=\left(f_{\overline{\alpha}}^*(\boldsymbol{x}+\delta\boldsymbol{x}_\alpha,t)-f_\alpha^*(\boldsymbol{x},t)\right)A_\alpha\delta x^2 \tag{13}$$

where $\boldsymbol{e}_{\overline{\alpha}}=-\boldsymbol{e}_\alpha$; f_α^* is the post-collision DF; and A_α denotes the face fill level determined by the averaged ε of cells at $\boldsymbol{x}$ and $\boldsymbol{x}+\delta\boldsymbol{x}_\alpha$

$$A_\alpha=\begin{cases}0 & \text{if cell } at\ \boldsymbol{x}+\delta\boldsymbol{x}_\alpha \text{ is gas}\\ \dfrac{\varepsilon(\boldsymbol{x})\varphi(\boldsymbol{x})+\varepsilon(\boldsymbol{x}+\delta\boldsymbol{x}_\alpha)\varphi(\boldsymbol{x}+\delta\boldsymbol{x}_\alpha)}{2} & \text{if cell } at\ \boldsymbol{x}+\delta\boldsymbol{x}_\alpha \text{ is interface}\\ \dfrac{\varphi(\boldsymbol{x})+\varphi(\boldsymbol{x}+\delta\boldsymbol{x}_\alpha)}{2} & \text{if cell } at\ \boldsymbol{x}+\delta\boldsymbol{x}_\alpha \text{ is liquid}\end{cases} \tag{14}$$

In the present single-phase VOF model, the free surface dynamic boundary condition (FSK) proposed by Korner et al [15] is applied here to reconstruct those missing distributions from gas phase without valid information,

$$f_{\overline{\alpha}}(\boldsymbol{x},t+\delta t)=-f_\alpha^*(\boldsymbol{x},t)+f_\alpha^{\mathrm{eq}}(\rho_{\mathrm{G}},\boldsymbol{u}_{\mathrm{G}})+f_{\overline{\alpha}}^{\mathrm{eq}}(\rho_{\mathrm{G}},\boldsymbol{u}_{\mathrm{G}}) \tag{15}$$

where $\boldsymbol{u}_{\mathrm{G}}$ is the free surface velocity extrapolated from fluid nodes. Within modified-pressure LBM scheme described above in Eq. (7), the present fluid pressure or density fields solved is the dynamic pressure. Therefore, the pressure at gas-liquid interface ρ_{G} is not a constant but is expressed as $\rho_{\mathrm{G}}=\rho_0-\rho_0\boldsymbol{g}(\boldsymbol{x}-\boldsymbol{x}_{\mathrm{ref}})/c_s^2$, rather than $\rho_{\mathrm{G}}=\rho_0$.

Once the mass exchange and DFs reconstruction are completed, the volume fraction ε can be updated by Eq. (11). If new ε exceeds 1, the interface cell is marked as filled and the neighbouring gas cells of those filled cells change to new-interface cells for closing the gas-liquid interface. In contrast, the interface cell is marked as emptied if ε is lower than 0 and its liquid neighbours change to interface cells. Consequently, a new free interface layer can be generated.

New-interface cells need to be initialized as previous gas cells do not contain valid information. The macroscopic velocity is interpolated from neighbouring liquid and interface cells as follows,

$$\begin{cases} \overline{\rho}(\boldsymbol{x}, t+\delta t) = \sum_{\alpha} w_{\alpha} \rho(\boldsymbol{x}+\delta \boldsymbol{x}_{\alpha}, t+\delta t) \Big/ \sum_{\alpha} w_{\alpha} \\ \overline{\boldsymbol{u}}(\boldsymbol{x}, t+\delta t) = \sum_{\alpha} w_{\alpha} \boldsymbol{u}(\boldsymbol{x}+\delta \boldsymbol{x}_{\alpha}, t+\delta t) \Big/ \sum_{\alpha} w_{\alpha} \end{cases} \tag{16}$$

Then the density distribution functions are initialized by equilibrium DFs as expressed in Eq. (4). The non- equilibrium term is obtained by a consistent initial condition proposed by Mei et al [44] to improve the accuracy. It is an iterative procedure: initialized as above, the collision and stream are implemented at the new-interface cells and then we update the local density but keep velocity constant. The iteration ends up in stable density field at those new-interface cells as,

$$\sum_{\boldsymbol{x}} \frac{|\rho(t+\delta t) - \rho(t)|}{|\rho(t+\delta t) + \rho(t)|} < \delta \tag{17}$$

where δ is a tiny quantity as the convergence criteria. Finally, DFs are taken as f_{α}^{*} after collision before streaming process.

Concerning the mass conservation, the excess mass from emptied ($\varepsilon < 0$) and filled ($\varepsilon > 1$) cells needs to be allocated to neighbouring interface and new-interface cells. Several distribution weight methods have been developed such as velocity-based [18], normal direction-based [15]. In present study, the normal direction-based algorithm is applied,

$$m(\boldsymbol{x}+\delta \boldsymbol{x}_{\alpha}) = m(\boldsymbol{x}+\delta \boldsymbol{x}_{\alpha}) + m^{\text{ex}} \frac{\nu_{\alpha}}{\nu_{\text{total}}} \tag{18}$$

$$\begin{gathered} \nu_{\alpha} = \begin{cases} \boldsymbol{n} \cdot \boldsymbol{e}_{\alpha}, & \text{if } \boldsymbol{n} \cdot \boldsymbol{e}_{\alpha} > 0 \\ 0, & \text{otherwise} \end{cases} \quad \text{for filled cells} \\ \nu_{\alpha} = \begin{cases} -\boldsymbol{n} \cdot \boldsymbol{e}_{\alpha}, & \text{if } \boldsymbol{n} \cdot \boldsymbol{e}_{\alpha} < 0 \\ 0, & \text{otherwise} \end{cases} \quad \text{for emptied cells} \end{gathered} \tag{19}$$

$$\boldsymbol{n} = \sum_{\alpha} - s_{\alpha} \boldsymbol{e}_{\alpha} \varepsilon(\boldsymbol{x}+\delta \boldsymbol{x}_{\alpha}) \tag{20}$$

where excess mass $m^{\text{ex}} = \rho$ for emptied cells and $m^{\text{ex}} = m - \rho$ for filled cells; ν_{total} is the sum of all weight ν_{α}; and $\boldsymbol{n}$ is the normal direction of the free interface. Finally, cells marked as transition state are converted into their final state, that is to say, Emptied, Filled, and New-interface cells are converted to gas, liquid, and interface cells, respectively. More details can be found in [15].

In fact, Eq. (14) corresponds to the averaging of the fill levels of two adjacent cells to approximate the face fill level. However, this implementation may lead to free surface oscillations, as it does not accurately capture the wetted interface between the cells [18]. To address this issue, the PLIC is adopted to determine the face fill level more precisely by which the mass flux term Δm_{α} is not only associated with the hydrodynamic quantities (i.e., $\boldsymbol{u}, f_{\alpha}$), but also the functions of geometrical parameters, namely the normal direction n and line parameter k calculated from ε [18,45], i.e. $\Delta m_{\alpha} = V(\boldsymbol{n}, k, f_{\alpha})$. In a 2D model, PLIC assumes that the free surface in each interface cells can be approximated as a line segment defined by $\boldsymbol{n} \cdot \boldsymbol{x} = k$. To determine the face fill level is in fact to calculate the intersections between the line and the four edges of interface cell. Referring to the 2D inverse problem [45], the line parameter k can be analytically obtained as follows,

$$k = \begin{cases} \sqrt{2m(1-m)\varepsilon} & 0 \le \varepsilon \le \varepsilon_1 \\ \varepsilon(1-m) + \dfrac{m}{2} & \varepsilon_1 \le \varepsilon \le 0.5 \end{cases} \tag{21}$$

where $m = \min\{\text{abs}(n_x, n_y)/(\text{abs}(n_x) + \text{abs}(n_y))\}$ and critical volume $\varepsilon_1 = \frac{m}{2(1-m)}$.

When the equation of straight line is determined, the face fill level can be calculated easily at each interface cell. For negative normal directions, the linear transformation and mirror reflection is applied so that all situations are generalized to the same problem solved as above. Different from the hybrid VOF-based algorithm described in [18], this study uses the DFs-based mass exchange for computational efficiency and stability, i.e., eight lattice directions for mass advection are used as in Eq. (13). The face fill level (regarded as the wet area between two cells) at orthogonal directions ($|e_{\alpha}|^2 = 3c_s^2$) is evaluated according to PLIC, but that at diagonal directions is calculated by averaged fill level of two cells where mass exchanges with diagonal cells ($|e_{\alpha}|^2 = 6c_s^2$).

2.3. Fluid-structure treatment

The bounce back scheme is imposed at liquid-solid boundary to reconstruct the unknown DFs from solid. As represented in Fig. 1, if the neighbouring node at $\boldsymbol{x}_{\text{f}} = \boldsymbol{x} + \boldsymbol{e}_{\overline{\alpha}} \delta t$ and $\boldsymbol{x}_{\text{ff}} = \boldsymbol{x} + 2\boldsymbol{e}_{\overline{\alpha}} \delta t$ is not gas cell, the united interpolated bounce back (UIBB) scheme [46] is implemented, otherwise the simple bounce back (SBB) is applied.

$$f_{\overline{\alpha}}(\boldsymbol{x}, t+\delta t) = \begin{cases} \dfrac{2}{(1+q)(2+q)} f_{\overline{\alpha}}(\boldsymbol{x}_{\text{w}}, t+\delta t) + \dfrac{2q}{(1+q)} f_{\overline{\alpha}}^{*}(\boldsymbol{x}, t) - \dfrac{q}{(2+q)} f_{\overline{\alpha}}^{*}(\boldsymbol{x}_{\text{f}}, t) & \text{Quadratic UIBB} \\ \dfrac{1}{1+q} \left(f_{\overline{\alpha}}(\boldsymbol{x}_{\text{w}}, t+\delta t) + q f_{\overline{\alpha}}^{*}(\boldsymbol{x}, t) \right) & \text{Linear UIBB} \\ f_{\alpha}^{*}(\boldsymbol{x}, t) - 2 w_{\alpha} \rho_{\text{w}} \boldsymbol{e}_{\alpha} \cdot \boldsymbol{u}_{\text{w}} & \text{SBB} \end{cases} \tag{22}$$

with

$$f_{\overline{\alpha}}(\boldsymbol{x}_{\text{w}}, t+\delta t) = \begin{cases} \left(\dfrac{q(1+q)}{2} f_{\alpha}^{*}(\boldsymbol{x}, t) + (1-q)(1+q) f_{\alpha}^{*}(\boldsymbol{x}_{\text{f}}, t) - \dfrac{(1-q)q}{2} f_{\alpha}^{*}(\boldsymbol{x}_{\text{ff}}, t) - 2 w_{\alpha} \rho_{\text{w}} \boldsymbol{e}_{\alpha} \cdot \boldsymbol{u}_{\text{w}} \right) & \text{Quadratic} \\ \left(q f_{\alpha}^{*}(\boldsymbol{x}, t) + (1-q) f_{\alpha}^{*}(\boldsymbol{x}_{\text{f}}, t) - 2 w_{\alpha} \rho_{\text{w}} \boldsymbol{e}_{\alpha} \cdot \boldsymbol{u}_{\text{w}} \right) & \text{Linear} \end{cases}$$

where the distance q is defined as $q = |\boldsymbol{x} - \boldsymbol{x}_{\text{w}}| / |\boldsymbol{e}_{\alpha} \delta t|$, $\boldsymbol{u}_{\text{w}}$ is the solid boundary velocity at $\boldsymbol{x}_{\mathrm{w}}$ and ρ_{w} is the solid boundary density, estimated as local liquid density $\rho(\boldsymbol{x}, t)$ in present nearly incompressible flows.

The change of momentum between post-collision $f_\alpha^*(\boldsymbol{x}, t)$ and post-streaming $f_{\overline{\alpha}}(\boldsymbol{x}, t+\delta t)$ denotes the discrete net force from solid to liquid in the momentum-exchange method (CMEM). For a stationary structure, the CMEM is the same as GIMEM,

$$\boldsymbol{F}_{\overline{\alpha}}(\boldsymbol{x}, t+\delta t) = \frac{\delta x^2}{\delta t}\left(f_{\overline{\alpha}}(\boldsymbol{x}, t+\delta t)\ \boldsymbol{e}_{\overline{\alpha}} - f_\alpha^*(\boldsymbol{x}, t)\boldsymbol{e}_\alpha\right) \tag{23}$$

where $\boldsymbol{e}_\alpha$ is the discrete velocity pointed to solid nodes; $\boldsymbol{x}_{\mathrm{w}}$ is the intersection of links and solid boundary. In the case of the fully immersed solid represented by the magenta nodes in Fig. 1, the contribution of atmospheric pressure to the hydrodynamic forces cancels out and hydrostatic buoyancy equal to $\rho g V_{\mathrm{s}}$. However, for a partially submerged structure represented by the grey coloured nodes in Fig. 1, the contribution of atmospheric pressure and hydrostatic buoyancy depend on the submerged depth, therefore we need to eliminate the effect of atmospheric pressure and correctly take hydrostatic pressure gradient (due to gravity) into account in the present LBM model. One correction introducing the equilibrium distribution function $f_\alpha^{\mathrm{eq}}(\rho_{\mathrm{G,w}},\ \boldsymbol{u}_{\mathrm{w}})$ into CMEM is expected to eliminate the contribution of atmospheric pressure and correctly evaluate the hydrostatic buoyancy force,

$$\boldsymbol{F}_{\overline{\alpha}} = \varepsilon\frac{\delta x^2}{\delta t}\left(\left(f_{\overline{\alpha}}(\boldsymbol{x}, t+\delta t) - f_{\overline{\alpha}}^{\mathrm{eq}}\right)\ \boldsymbol{e}_{\overline{\alpha}} - \left(f_\alpha^*(\boldsymbol{x}, t) - f_\alpha^{\mathrm{eq}}\right)\boldsymbol{e}_\alpha\right) \tag{24}$$

where $\rho_{\mathrm{G,w}}$ is the fluid density at position $\boldsymbol{x}_{\mathrm{w}}$, $\rho_{\mathrm{G,w}} = \rho_0 - \rho_0\boldsymbol{g}(\boldsymbol{x}_{\mathrm{w}} - \boldsymbol{x}_{\mathrm{ref}})/c_s^2$.

Then the total hydrodynamic forces acting on the object are summed as,

$$\boldsymbol{F} = -\sum_{\boldsymbol{x}}\sum_{G(\boldsymbol{x})}\boldsymbol{F}_{\overline{\alpha}}(\boldsymbol{x}, t+\delta t) \tag{25}$$

where the set $G(\boldsymbol{x})$ includes all discrete direction α that link to solid nodes at the non-solid node $\boldsymbol{x}$.

2.4. *Wave generation and absorption*

To explore the capability of the present model in a dynamic scenario, a numerical wave tank (NWT) is developed, as shown in Fig. 3, including wave generation and absorption techniques,

Stoke waves are generated by a classic momentum source [21,47] in the generation region, and the equivalent source term $\boldsymbol{S}_{\mathrm{g}}$ is,

$$\begin{cases} S_{\mathrm{g},x} = g(2\beta(x - x_{\mathrm{s}}))e^{-\beta(x-x_{\mathrm{s}})^2}\dfrac{\delta}{\omega}\sin\omega t \\ S_{\mathrm{g},y} = 0 \end{cases} \tag{26}$$

where g is the gravity acceleration and $\beta = 20/W^2$ is a coefficient of source width W; x_{s} is the centre of wave generating area; δ is distribution source density,

$$\delta = \frac{2A\left(\omega^2 - \alpha_1 g k^4 d^3\right)}{\omega I k\left(1 - \alpha(kd)^2\right)} \tag{27}$$

where A is the wave amplitude; α =-0.38955 and $\alpha_1 = \alpha + 1/3$ is a coefficient of the basic Boussinesq equation; d is the still water depth; $k = 2\pi/L$ is the wavenumber and L is the wavelength; $I = \sqrt{\pi/\beta}e^{-k^2/4\beta}$.

Concerning reflected waves from both ends of NWT, numerical damping layer (sponge layer) is imposed to achieve wave attenuation. In the absorption region with width L_{s}, the damping force $\boldsymbol{S}_{\mathrm{d}}$ is given as,

$$\boldsymbol{S}_{\mathrm{d}}(t+\delta t) = -B_1\boldsymbol{u}(t)\frac{e^{\left|\frac{x-x_0}{L_{\mathrm{s}}}\right|^{n_{\mathrm{s}}}} - 1}{e - 1} \tag{28}$$

where B_1 and n_{s} are empirical coefficients, and x_0 is the starting location of the sponge layer.

In Eq. (28), the damping force is evaluated by the water fluid velocity at the last time step. To avoid the resulting instability and error, we introduce the force source term into equilibrium DFs so that $\boldsymbol{S}_{\mathrm{d}}$ can be calculated from velocity at current time step. Then the equilibrium distribution functions f_α^{eq} is expressed as in the absorption region,

$$f_\alpha^{\mathrm{eq}}(\boldsymbol{x}, t) = w_\alpha\rho\left[1 + \left(1 + \frac{\chi}{\omega_\nu}\right)\frac{\boldsymbol{e}_\alpha\cdot\boldsymbol{u}}{c_s^2} + \left(1 + \frac{2\chi}{\omega_\nu}\right)\left(\frac{(\boldsymbol{e}_\alpha\cdot\boldsymbol{u})^2}{2c_s^4} - \frac{\boldsymbol{u}^2}{2c_s^2}\right)\right] \tag{29}$$

where $\chi = -B_1\frac{e^{\left|\frac{x-x_0}{L_{\mathrm{s}}}\right|^{n_{\mathrm{s}}}} - 1}{e-1}$. In wave absorption region, substituting Eq. (29) into (3),

$$\begin{cases} \boldsymbol{m}^{\mathrm{eq}} = \rho A_{\mathrm{d}}\bullet\left[1,\ \left(1 + \dfrac{2\chi}{\omega_e}\right)\boldsymbol{u}^2 - 2,\ 1 - \left(1 + \dfrac{2\chi}{\omega_\epsilon}\right)\boldsymbol{u}^2,\ u_x, -u_x, u_y, -u_y, u_x^2 - u_y^2, u_x u_y\right]^{\mathrm{T}} \\ A_{\mathrm{d}} = diag\left(\left[1,\ 1,\ 1,\ 1 + \chi, 1 + \dfrac{\chi}{\omega_q}, 1 + \chi, 1 + \dfrac{\chi}{\omega_q}, 1 + \dfrac{2\chi}{\omega_\nu}, 1 + \dfrac{2\chi}{\omega_\nu}\right]\right) \end{cases} \tag{30}$$

2.5. *Implementation and performance*

The development of the proposed LBM model relies on the open-source multi-platform lattice Boltzmann code (MPLB), which is a backend code of the High-Level Mesoscale Modelling System (HiLeMMS) project (EP/P022243/1) supported by the Engineering and Physical Sciences Research Council (EPSRC) of the UK Research and Innovation under the UK Consortium on Mesoscale Engineering Sciences (UKCOMES) [48].

The HiLeMMS is a computational framework designed to provide a high-level abstraction system for LBM. It hides the low-level implementation details (e.g., MPI) for utilizing high-performance computing resources, simplifies parallel programming and enables researchers to focus on physical modelling and numerical analysis. Its detailed description can be found at GitHub: https://github.com/inmeso/hilemms.git.

As a backend code of HiLeMMS, MPLB is written by using the oxford parallel library for structured mesh solvers (OPS) [49], which provides the mesh management for parallel computing and the capability of running on a heterogeneous computing platform. MPLB has been utilized in a range of applications, including shallow water flows [50], particle-fluid two-phase flows [51,52].

In this study, we focus on fluid flows consisting of two immiscible Newtonian fluids and the coupling with partially submerged structures, which involve an algebraic VOF algorithm for capturing sharp interface between phases and IBB-MEM algorithm for fluid-solid boundary treatment. The implementation of these algorithms is based on MPLB and the source has been made publicly available at https://github.com/BaomingGuo/mplb.git. The structure of the code is briefly illustrated in Fig. 4, and more details about the workflow are given as follows.

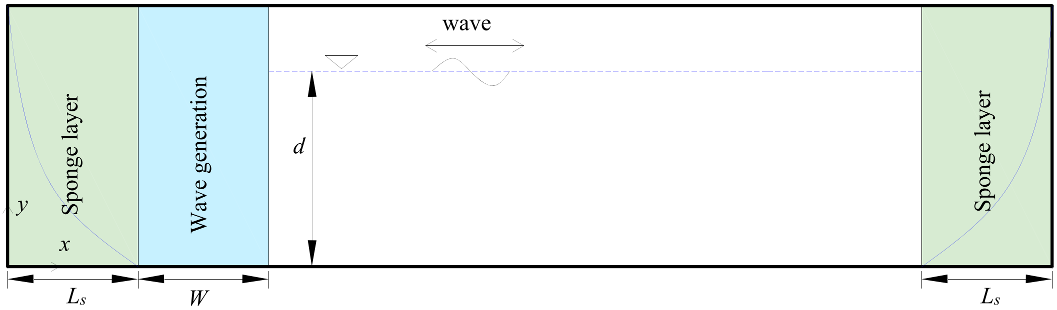

Fig. 3. Schematic diagram for a numerical wave tank.

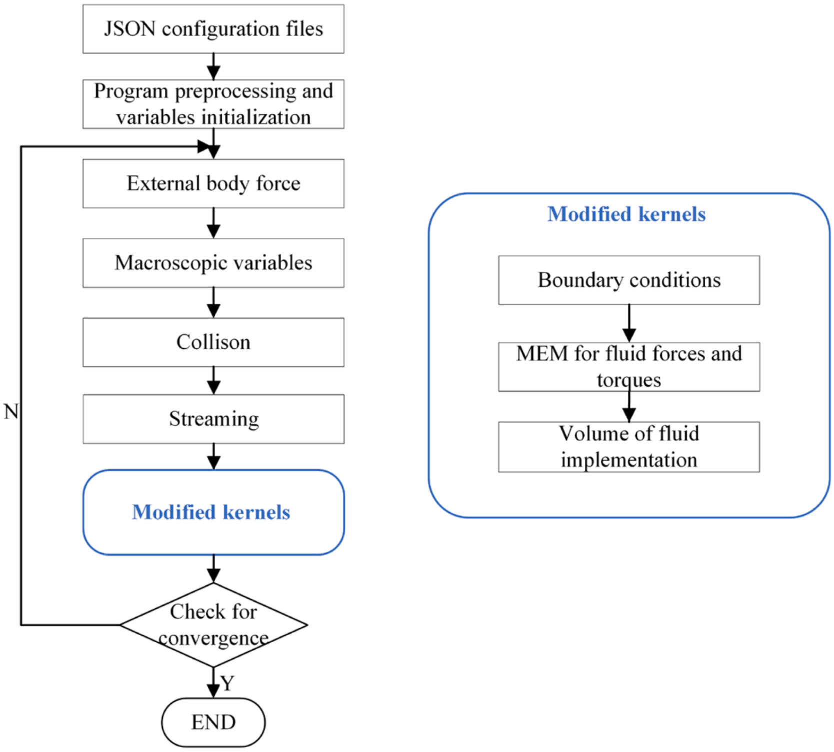

Fig. 4. Flowchart of the LBM program structure. More details can be found at the numbered list above.

1). Input user parameters via JSON configuration files. These parameters typically include geometry settings, domain size, mesh resolution, convergence criteria, etc.

Preprocessing,

1). Define the problem domain, macroscopic variable types, and body force schemes, and domain boundary types.
2). Decompose the computational domain onto allocated CPU processors and memory space, and set halo points. These operations are automatically managed by HiLeMMS and MPLB.
3). Set node types for all grid nodes, including empty (gas), liquid, interface, solid, boundary conditions.
4). Initialize all variables, including macroscopic variables derived from DFs (e.g., density, velocity) and auxiliary quantities (e.g., solid fraction, fluid fraction, relative distance).

From this point onward, the main time loop of the LBM simulation is executed,

1). Calculate the body force term at DF level: including a momentum source from wave generation and absorption, and updating the discrete force term using the Guo's force scheme, followed by updating the macroscopic variables, e.g., density and velocity.
2). Execute the collision step to compute post-collision DFs. Then, perform the streaming step to exchange DFs with neighbouring nodes.
3). Implement boundary conditions, including domain boundaries (e.g., outflow or no-slip wall), free surface Eq. (15), and fluid-solid boundaries Eq. (22).
4). Calculate momentum exchange for fluid nodes based on Eq. (24), and store the total hydrodynamic force acting on structures (see Algorithm 1).
5). Calculate mass exchange at interface nodes during the streaming step according to Eq. (13) (see Algorithm 2), (VOF).
6). Identify transmitted cells and predefine node types. Refill new interface cells and allocate excess mass accordingly (see Algorithm 3), (VOF).

Algorithm 1

Pseudo-code for calculating fluid forces by MEM (MomentumExchangeSolid in MPLB).

```
// ops_par_loop(KerUIBB_GIMEM, …) executes the kernel function in parallel over all grid nodes
if (node.type == LIQUID or node.type == INTERFACE) {
    for each lattice direction $\alpha$ {
        if (neighbor.type == SOLID) {
            sum up the discrete fluid force at the $\alpha^{\text{th}}$ direction computed by Eq. (24)
        }
    }
}
// Use ops_par_loop(KerTotalHydroForce, …) with ops_arg_reduce(…) to sum up total fluid forces
```

Algorithm 2

Pseudo-code for implementing mass exchange in VOF model (MassExchange).

```
// ops_par_loop(KerMassExchange, …)
if (node.type == INTERFACE) {
    for each lattice direction $\alpha$ {
        // according to neighbouring node state to compute convective mass
        Evaluate mass exchange $\Delta m_\alpha$ by Eqs. (13) and (14)
        Accumulate $\Delta m_\alpha$ into the liquid mass of this local interface cell
    }
}
```

Algorithm 3

Pseudo-code for implementing excess mass allocation in VOF model (AllocateMass).

```
// ops_par_loop(KerCalcTotalWeight, …) compute the total weights $\nu_{total}$ at each node
if (node.type == FILLED or node.type == EMPTIED) {
    for each lattice direction $\alpha$ {
        if (neighbor.type == INTERFACE) {
            Determine allocation weight $\nu_\alpha$ by Eq. (19)
        }
        Sum up $\nu_\alpha$ to calculate $\nu_{\text{total}}$
    }
}
// ops_par_loop(KerAllocateMassMpi, …) allocates excess mass
if (node.type == INTERFACE) {
    for each lattice direction $\alpha$ {
        if (neighbor.type == FILLED or neighbor.type == EMPTIED) {
            Determine allocation weight $\nu_\alpha$ by Eq. (19) using $-\boldsymbol{n}(\boldsymbol{x}+\delta\boldsymbol{x}_\alpha)\cdot\boldsymbol{e}_\alpha$
            Calculate excess mass $m^{\text{ex}}$
            modify Eq. (18) to avoid nonlocal write operation to update liquid mass $m(\boldsymbol{x}) += m^{\text{ex}}\frac{\nu_\alpha}{\nu_{\text{total}}}$
        }
    }
}
```

7). Update node states and calculate the volume fraction of liquid, (VOF).
8). Repeat 6) – 12) until the convergence criteria are satisfied.

In this code, as shown at the right-hand side of Fig. 4, each algorithm is implemented via a kernel function, which conducts a specific set of operations on a grid node and will be populated to the whole computational domain. These kernel functions in MPLB are presented below in the form of pseudo-codes.

The numerical simulations are conducted on ARCHER2 HPC cluster (UK National Supercomputing Service). To evaluate the code performance, an NWT case is simulated using different numbers of computational nodes on ARCHER2. The wave period and amplitude are 1 s and 0.01 m, respectively, with a still water depth of 0.2 m. The 2D case consists of 4.32 million structured grids (18,000 × 240). The wave generation domain, spanning one wavelength (as shown in Fig. 5), is positioned at the center, and the sponge layer extending two wavelengths is placed only at the right-hand end of the NWT to absorb outgoing waves.

Fig. 5 (a) and (b) illustrate the free surface elevation in different domains, along with the velocity fields in the left region. As expected, the superposition of incident and reflected waves on the left-hand side results in the formation of standing waves, whereas the right-hand side exhibits a train of progressive waves. Fig. 5 (c) and (d) present the parallel speed-up ratio and efficiency in a strong scaling test. For a 2D case with approximately four million grids, the free surface LBM model implemented in HiLeMMS achieves 90 % parallel efficiency using 1024 CPUs, demonstrating its good parallel scalability.

Moreover, the scalability of the LBM model is analyzed through weak scaling tests. Table 1 lists the wall time of different tank lengths. When the number of CPU cores increases in proportion to the total number of grid cells, the single-core performance of the solver remains nearly unaffected. This indicates that the current LBM-based NWT can efficiently handle large-scale problems by scaling up the number of CPU cores.

3. Model validation

The model validation is structured in three progressive stages: single-phase flows over fully submerged structures, pure free surface flows, and free surface flows over partially submerged structures, which correspond to five benchmark cases including flow over a circular cylinder [53–59], flow over a square cylinder [60–63], Rider-Kothe single vortex evolution [18,64], dam-break flows [65], and wave impact on stationary structures [2,3]. The steady and unsteady flows with different Reynolds numbers (*Re*) over the circular and square cylinders are first studied, which are compared with published experimental and numerical results.

3.1. Flow over a circular cylinder

The flow past a circular cylinder has been extensively studied by many researchers. With the Reynolds number defined by $\text{Re} = u_0 D/\nu$, the steady flow is generated with two symmetric vortexes behind the cylinder when Re is lower than the critical value ($\text{Re}_{\text{cr}} \approx 47$), where u_0 and D are the freestream velocity at far distance and cylinder diameter, respectively. The unsteady laminar flow is then obtained when *Re* exceeds the critical value and the periodic vortex shedding occurs. In this study, the lift, drag coefficients and Strouhal number are evaluated for comparison with published results: Drag coefficient $C_{\text{D}} = 2F_{\text{D}}/(u_0^2 D)$, lift coefficient $C_{\text{L}} = 2F_{\text{L}}/(u_0^2 D)$, and dimensionless shedding frequency $S_{\text{t}} = f_{\text{q}} D/u_0$.

In this case, a rectangular simulation domain is set as $50D \times 30D$ The inlet boundary is imposed with the velocity inlet with uniform profile ($u_0 = 1$), and a second-order time implicit convective boundary condition (CBC) [66] is imposed on the outlet boundary, expressed by Eq. (31) for avoiding boundary reflection. To simulate uniform flows, the symmetrical condition is implemented for the top and bottom free-slip walls. The center of circular cylinder is located at $x = y = 0$ in the computational domain ($-20D \le x \le 30D$ and $-15D \le y \le 15D$). The uniform grid is adopted with grid resolution $D/32$ and the grid is thus 1600 × 960 for both flows characterized by Re =40 and 100.

$$f_\alpha(\boldsymbol{x}_{\text{N}}, t+\delta t) = \frac{1}{1+1.5\gamma}\left(f_\alpha(\boldsymbol{x}_{\text{N}}, t) + 2\gamma f_\alpha(\boldsymbol{x}_{\text{N}-1}, t+\delta t) - 0.5\gamma f_\alpha(\boldsymbol{x}_{\text{N}-2}, t+\delta t)\right) \tag{31}$$

where $\gamma = u_0/c_s$ and $\boldsymbol{x}_{\text{N}}$ is the outlet boundary node and $\boldsymbol{x}_{\text{N}-1}$ and $\boldsymbol{x}_{\text{N}-2}$ are the neighbouring liquid nodes towards negative normal direction.

Fig. 6 shows the streamline and vortex contours of the flows at Reynolds numbers of 40 and 100, where dimensionless vorticity is $\omega D/u_0$ and the dimensionless time was defined as $T = u_0 t/D$. At Re =40, the flow is stable with good symmetricity on both sides of the central line, but at Re =100, the streamlines become wavy, and flow is asymmetrical. Strong vortex shedding in the wake of the cylinder is formed. The comparisons of the drag coefficient (C_{D}), the length of bubble recirculation (L) and the distance between two vortices (b) with the

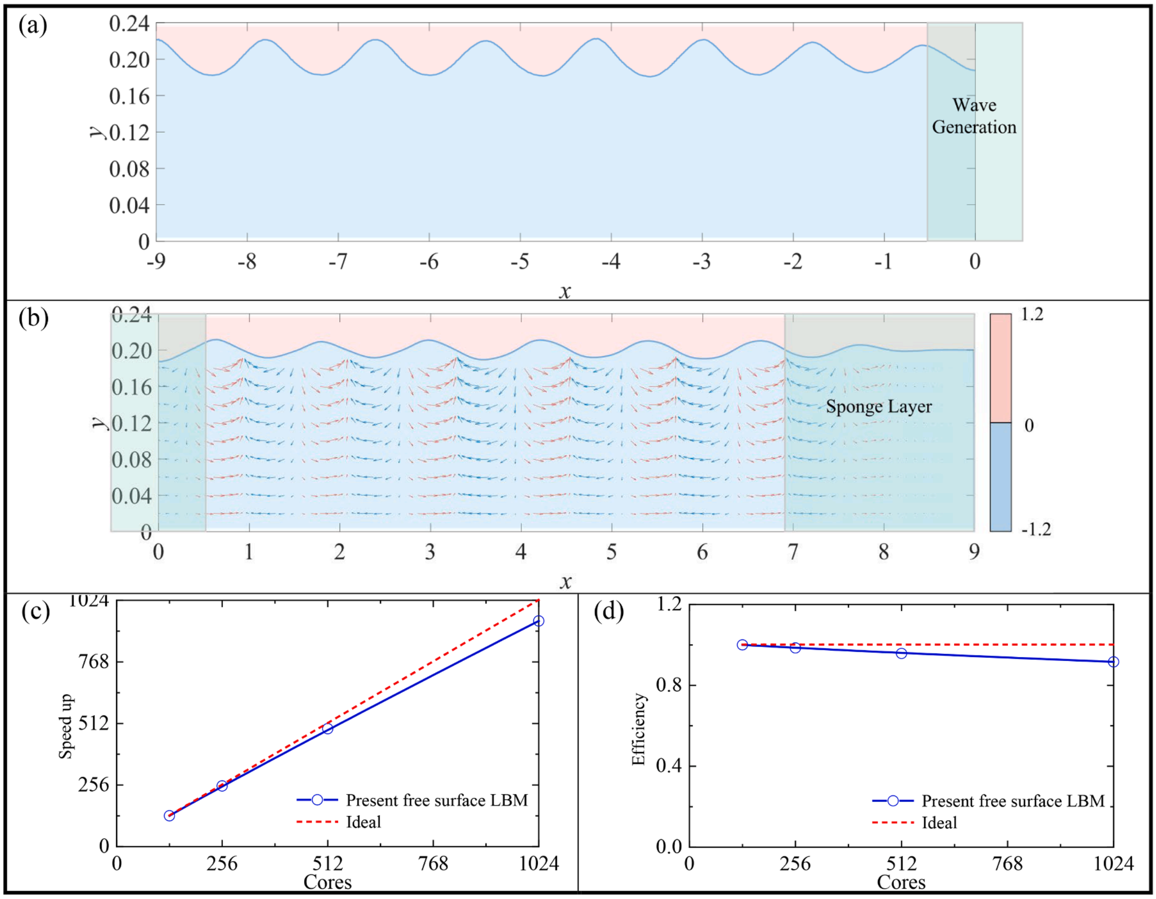

Fig. 5. Performance test of free surface LBM model through a numerical wave tank case. (a) Standing waves in the left-hand side of NWT, (b) progressive waves in the right-hand side of NWT, and (c)&(d) the parallel speed-up ratio from strong scaling tests conducted using 1, 2, 4 and 8 nodes, where each node on Archer2 comprises 128 CPU cores.

Table 1
Wall time required to complete 0.4-million time steps for numerical wave tank (NWT) cases with varying tank lengths in the weak scaling tests.

CPU cores	Length of NWT (m)	Number of grid	Wall time (s)
128 (1 node)	18	18,000 × 240	20,332
256 (2 nodes)	36	36,000 × 240	20,375
512 (4 nodes)	72	72,000 × 240	20,413
1024 (8 nodes)	144	144,000 × 240	20,495

published results are listed in Table 2. It agrees well with other numerical and experimental results. where IBM and IIM are the immersed boundary method and immersed interface method, respectively.

3.2. Flow over a square cylinder

In addition to the circular cylinder, we also simulate the flow past a square cylinder to validate the stability of the present model when the uniform flow encounters sharp corners. The same simulation domain, initial flow field, and boundary conditions are set up as in the circle cylinder case. The resulting flow fields are depicted in Fig. 7 showing the streamline and vorticity near square cylinder. The averaged drag coefficient $\overline{C}_{\mathrm{D}}$, root mean square lift coefficient $C_{\mathrm{L,rms}}$, recirculation length L/D, and vortex shedding frequency S_{t} are compared in Table 3. In terms of hydrodynamic forces and vortex characteristics, the present LBM model agrees well with those published results. These results demonstrate that the LBM model can accurately solve the hydrodynamics of the square structure in steady and unsteady flows.

3.3. Rider-Kothe single vortex

To validate the capability of the model in tracking free surface, the Rider-Kothe single vortex test case [18,64] is carried out. Without solving Boltzmann-BGK equation, the simulation solutions of each iteration are specified as the equilibrium distribution functions instead, according to the streaming function in Eq. (32). It depicts a free surface deformation where one circular liquid drop twists into a spiral pattern and is gradually restored to the initial state after half a period. The initial circle centre is located at (0.5, 0.75) with the radius of 0.15 and period T is set as 2 in the 1 × 1 square domain.

$$\psi = \frac{u_0}{\pi}\sin^2\pi x\cdot\sin^2\pi y\cdot\cos\frac{\pi t}{T} \tag{32}$$

The Relative error between simulated and theoretical VOF is defined by,

$$E_{\mathrm{r}} = \frac{\delta x^2 \sum|\varepsilon_{\mathrm{s}} - \varepsilon_{\mathrm{theo}}|}{V_{\mathrm{theo}}} \tag{33}$$

where V_{theo} is the total theoretical liquid volume.

Fig. 8. shows the free surface deformation process with computational grid 512 × 512. It can be observed that the free surface deformations generally overlap between the first and last half-periods. With grid refinement, the present model can capture the 2D free interface well whether face fill levels are evaluated by average of ε or PLIC. Table 4 compares the errors between the results of different grid resolutions and face fill level evaluation methods, and the published

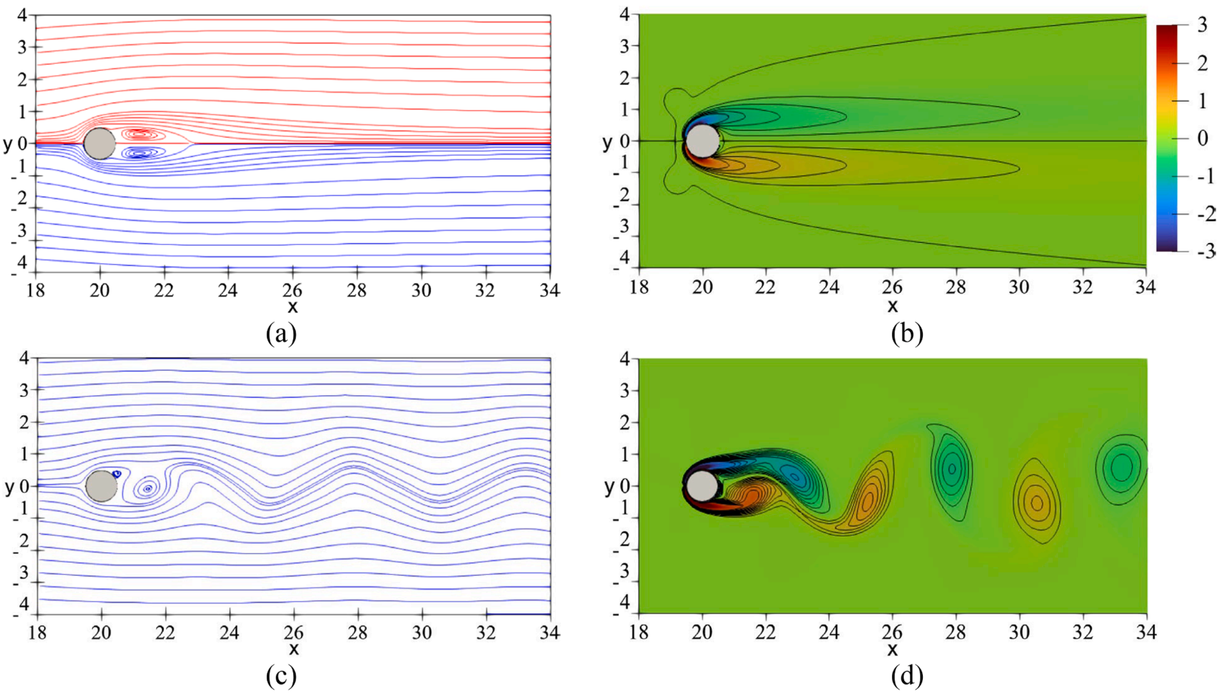

Fig. 6. The computed streamline and vorticity contour near circular cylinder at $T = 451$ within $50D \times 30D$ computational domain. (a) & (b) steady flow Re =40 and (c) & (d) unsteady flow Re =100.

Table 2
Comparison of the present study with the published results at Re = 40 and 100 for the flow past circular cylinder.

Study	Re = 40				Re =100		
	C_D	L/D	b		C_D	C_L	S_t
Experiment [53]	1.59	–	–	NS-based body-fitted [54]	1.35±0.012	±0.339	0.164
NS-based IBM [55]	1.54	2.30	0.6	NS-based IBM [56]	1.38±0.01	±0.34	0.169
NS-based IBM [57]	1.52	2.27	0.6	NS-based IBM [57]	1.35±0.012	±0.303	0.167
NS-based IIM [58]	1.54	2.28	0.6	NS-based IIM [58]	1.34±0.009	±0.333	0.166
NS-based cut-cell [59]	1.534	2.21	0.594	NS-based cut-cell [59]	1.33±0.009	±0.320	0.17
Present	1.555	2.25	0.594	Present	1.346±0.009	±0.325	0.167

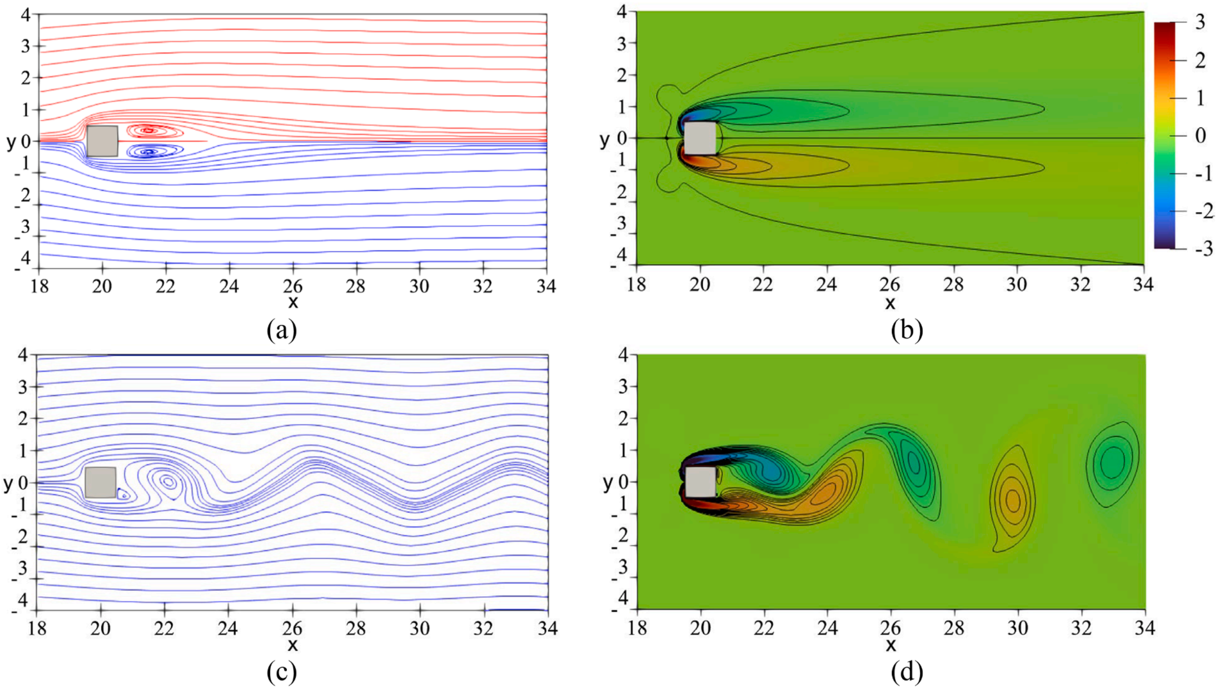

Fig. 7. The computed streamline and vorticity contour near square cylinder at $T = 451$ within $50D \times 30D$ computational domain. (a) & (b) steady flow Re =40 and (c) & (d) unsteady flow Re =100.

Table 3
Comparison of the present and well-published results at Re = 40 and 100 for flow past square cylinder.

Study	Re = 40				Re =100		
	$\overline{C}_{\mathrm{D}}$	L/D	b		$\overline{C}_{\mathrm{D}}$	$C_{\mathrm{L,rms}}$	S_{t}
NS-based FVM [60]	1.767	2.822	–	NS-based FVM [61]	1.477	0.156	0.146
NS-based FVM [62]	1.793	2.83	–	NS-based FVM [62]	1.494	0.192	0.149
NS-based FEM [63]	1.787	2.807	–	NS-based FEM [63]	1.529	0.193	0.145
Present	1.712	2.825	0.334	Present	1.479	0.188	0.144

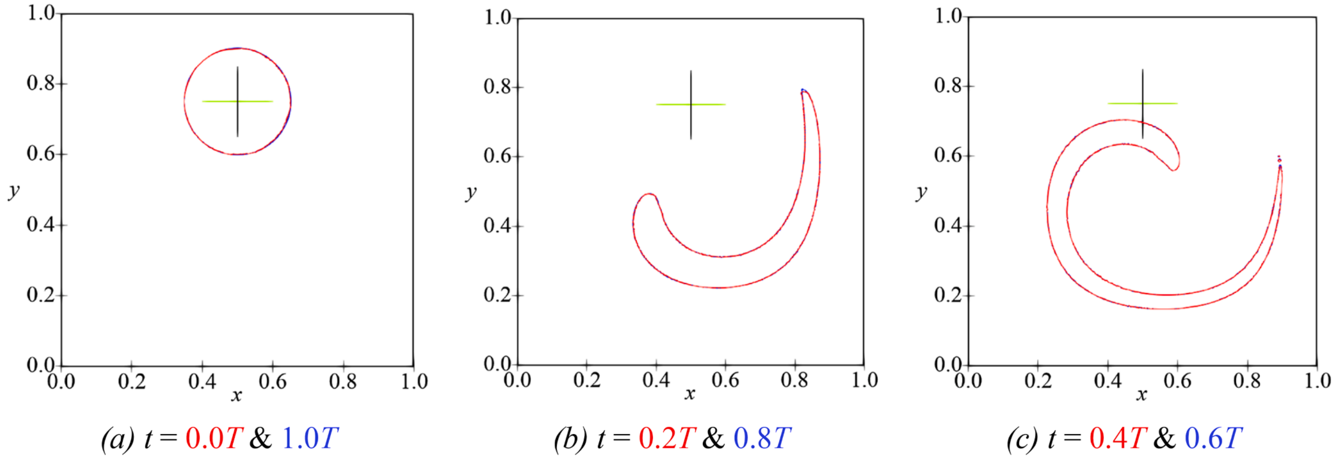

(a) $t = 0.0T$ & $1.0T$ (b) $t = 0.2T$ & $0.8T$ (c) $t = 0.4T$ & $0.6T$

Fig. 8. Snap shots of free surface deformation of Rider-Kothe vortex during one period with computational grid 512 × 512 and u_0 =2.

Table 4
Comparison of relative errors E_{r} for the single vortex case.

Study		E_{r}	
		average of ε	PLIC
u_0 =1	Rider and Kothe [64] (128 × 128)	–	0.2×10^{-2}
	Harvie and Fletcher [67] (128 × 128)	–	0.3×10^{-2}
	Present (128 × 128)	2.1×10^{-2}	1.5×10^{-2}
	Present (256 × 256)	1.2×10^{-2}	0.9×10^{-2}
	Present (512 × 512)	0.8×10^{-2}	0.5×10^{-2}
u_0 =2	Janssen and Krafczyk [18] (128 × 128)	5.6×10^{-2}	1.0×10^{-2}
	Present (128 × 128)	3.0×10^{-2}	2.1×10^{-2}
	Present (256 × 256)	2.1×10^{-2}	1.4×10^{-2}
	Present (512 × 512)	1.5×10^{-2}	0.9×10^{-2}

Table 5
Simulation setup for the dam break flow.

Domain	Lattice	Water height	Water width	Re = $\frac{U_{\max}a}{\nu}$	Fr = $\frac{U_{\max}}{\sqrt{ga}}$	C_s
$10a \times 2.5a$	1024 × 256	$2a$	a	103,483	2.42	0.1

numerical solutions (with grid resolution 128 × 128) [18,64,67]. Indeed, PLIC is better than averaged fill level, but the discrepancy is regarded acceptable between them for remaining the high computational efficiency. For all cases with PLIC, since the diagonal mass flux terms cannot be calculated accurately, the present model with DF-based mass exchange performs slightly worse than those models using macroscopic velocity-based mass exchange.

3.4. Dam-break flows

The classic benchmark for dam-break flows by Martin and Moyce [65] is used here to demonstrate the capability of the present model in simulating free surface flows. Martin and Moyce [65] determined a maximum dimensionless velocity $U^*_{\max} = U_{\max}/\sqrt{2ga} = 1.71$ in the water-column collapse. Table 5 gives parameters of model domain assuming initial water width (a) being 0.05715 m and kinematic viscosity (ν) being 10^{-6} m^2/s. In the present simulation, the slip boundary condition is imposed at all four boundaries with UIBB. Fig. 9 gives free surface deformation at four different moments, illustrating the collapsing water column moving forward. And then the positions of

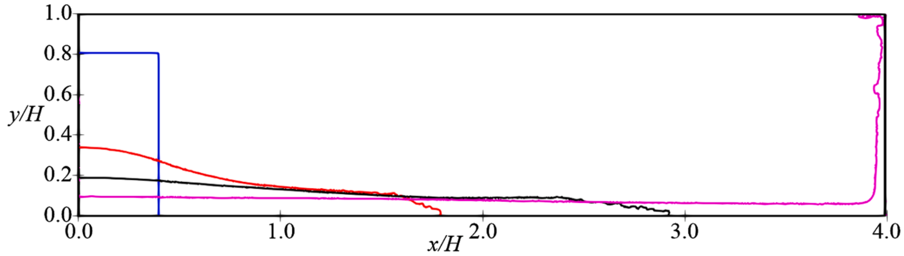

Fig. 9. Free surface deformation at different moments. Bule, red, black, and pink lines deonte the free surface at $t\sqrt{2g/a}$ = 0, 3.30, 4.96, and 7.91, respectively, where H is the height of the computational domain.

water column top and surge front for different grid resolutions against dimensionless time are shown in Fig. 10, compared with the numerical and experimental data from [65,68]. It can be observed that the present model agrees well with the numerical results by Greaves [68]. The predicted water column height shows good agreement with experimental results while the waterfront moves more quickly than that of the experiment. A similar discrepancy is observed in [18,68]. It is explained that it is difficult to determine the exact location of the waterfront in the experiment. The numerical results demonstrate that the present model is capable of simulating real free surface flows.

3.5. *Wave propagation through stationary boxes*

The final case for model validation is to simulate the waves passing through two closely adjacent stationary boxes (the upstream and downstream boxes are denoted as Box 1 and Box 2, respectively), where a wave-induced narrow gap resonance phenomenon is studied. As shown in Fig. 11, the draft of both boxes is 0.252 m and the breadth is 0.5 m, with a narrow gap of 0.05 m between the boxes. Table 6 gives all parameters for waves and NWT. The dimensionless LBM is referred to Re $= L/T \cdot d/\nu$. Here, the left and right boundaries are imposed as the Neumann outflow condition, and no-slip wall condition is implemented on the box and bottom boundaries. The wave response H_g in the narrow gap and hydrodynamic force on both bodies are evaluated with respect to experimental and numerical results in [2,3]. In addition, a theoretical potential-flow solution is given based on matching eigenfunction expansions for comparison. For brevity, details of this potential-flow model are shown in Appendix A.

Fig. 12 displays the time series of hydrodynamic forces exerted on two boxes at $kd = 1.5$. It can be observed that the present NWT can stably measure the hydrodynamic forces near narrow gap resonance frequency. This measurement stability is corroborated by the consistent and periodic wave elevation (with a period equal to the wave period) observed in the narrow gap, as shown in Fig. 13 (a). These findings together confirm the stability of the combination of IBB and VOF treatments. Then, the variation of wave amplitude in the narrow gap and hydrodynamic forces on both boxes against wave frequency are depicted in Fig. 13, Fig. 14, Fig. 15. The predicted variation trends of A_g and $|\boldsymbol{F}|$ are in good agreement with experimental [2,3] and numerical results [2] in which the fluid response near gap resonance frequency is the most

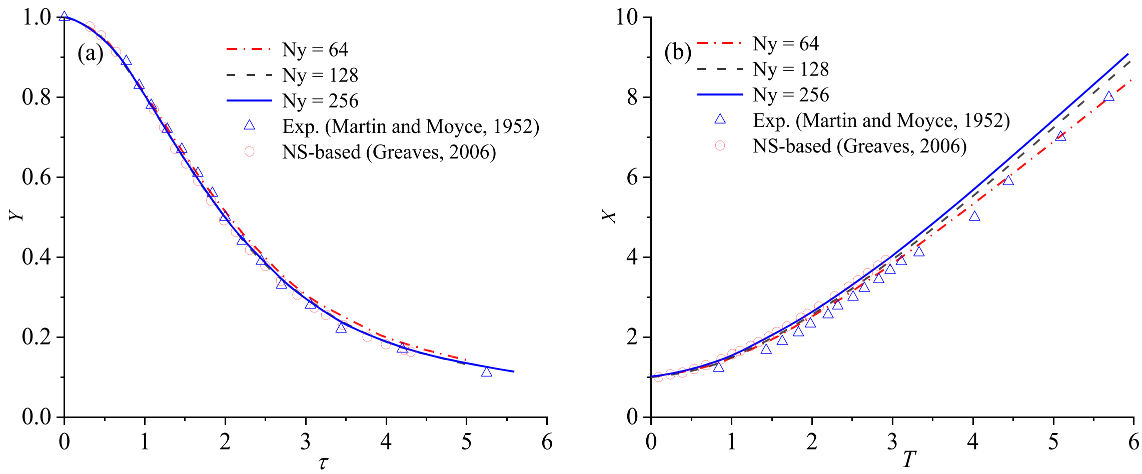

Fig. 10. Comparison of present LBM predictions, NS-based numerical results by Greaves [68], and experimental results by Martin and Moyce [65], where *Ny* is the grid number in the vertical direction. (a) Dimensionless water column height, $Y = y_{top}/2a$ and $\tau = t\sqrt{g/a}$, (b) position of water surge front $X = x_{front}/a$ and $T = t\sqrt{2g/a}$.

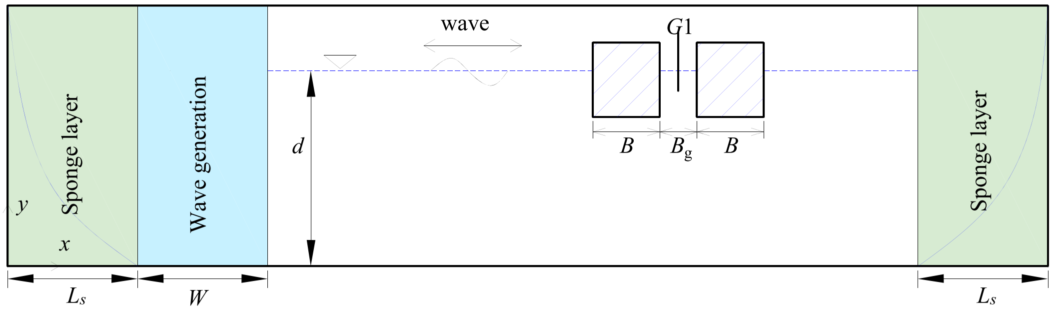

Fig. 11. Schematic diagram of two closely adjacent stationary boxes in the NWT.

Table 6
The parameters of NWT in Fig. 11.

Waves	L (m)	T (s)	H (m)	d (m)	NWT	Length (m)	Height (m)
	1.05~3.14	0.82~1.63	0.024	0.5		10L	1.3d
Wave Absorption	B_1 (s^{-1})	n_s	L_s (m)		Wave Generation	W (m)	
	20	2	2L			L	
Boxes	D (m)	B (m)	B_g (m)		Subgrid-scale model	C_s	
	0.252	0.5	0.05			0.1	

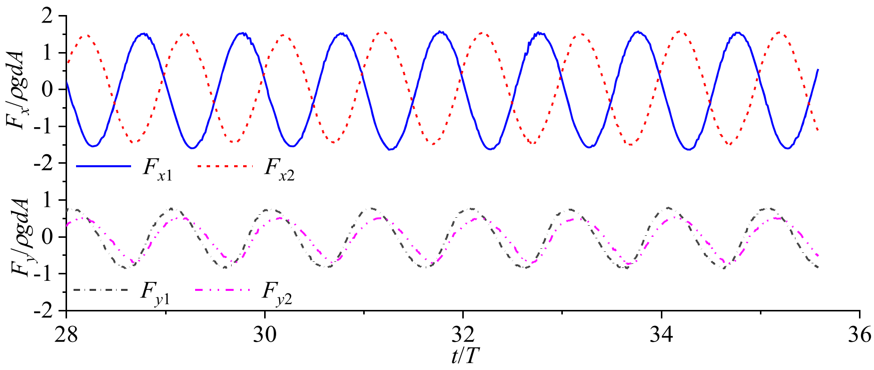

Fig. 12. Time series of hydrodynamic forces on Box 1 and 2 at kd =1.5.

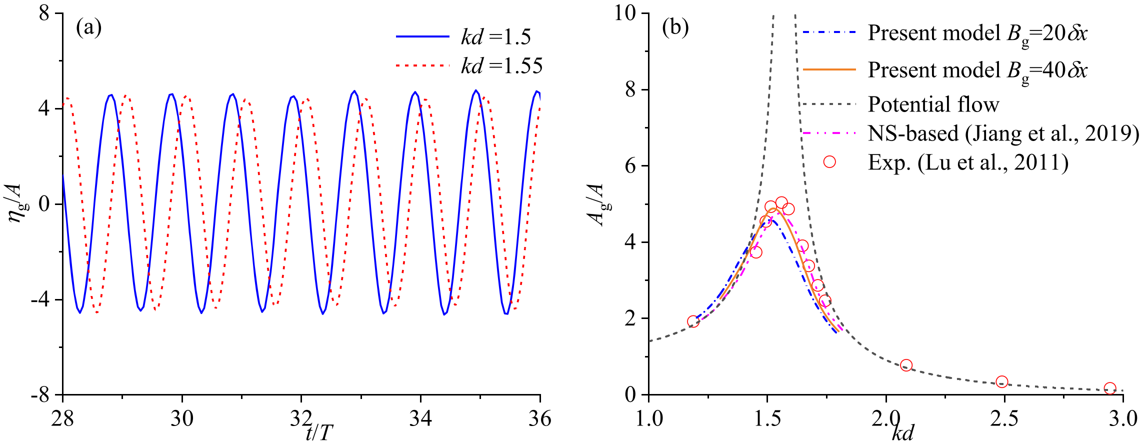

Fig. 13. (a) Time series of free surface elevation in the gap at kd =1.5 and 1.55. (b) Comparison of wave amplitude inside the gap versus dimensionless wavenumbers obtained from the present model, NS-based model by Jiang et al [2], and experiment by Lu et al [3].

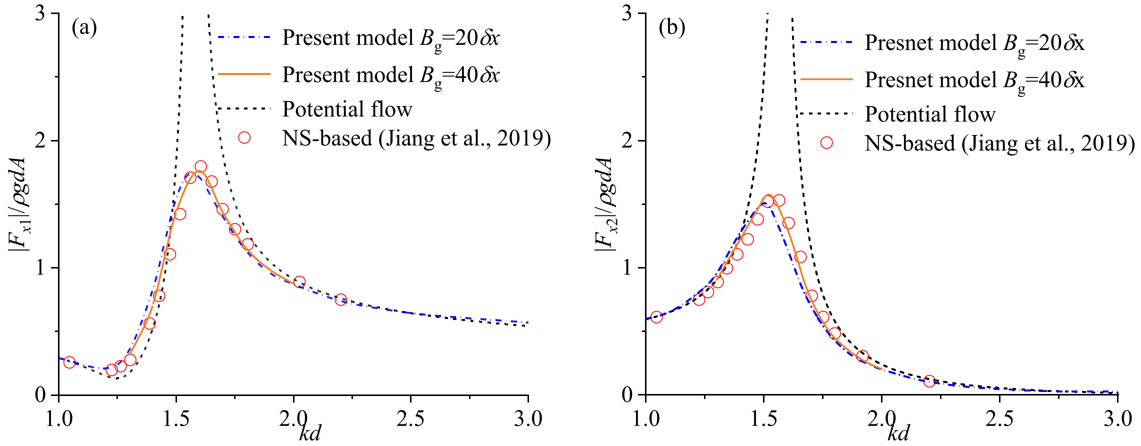

Fig. 14. Comparison of horizontal forces on Box 1 and Box 2 versus dimensionless wavenumbers obtained from the present model, NS-based model by Jiang et al [2]: (a) $|F_{x1}|/\rho gdA$ and (b) $|F_{x2}|/\rho gdA$.

violent within the calculated frequency interval. Owing to their ability to capture nonlinear and viscous fluid behavior, the LBM and NS-based CFD models offer significantly improved quantitative agreement with experimental measurements, compared with linear potential-flow solutions.

The present LBM framework exhibits good agreement with experimental measurements and NS-based numerical results, in predicting both water surface elevation and hydrodynamic forces. However, a noticeable discrepancy is observed in capturing the resonant response, particularly in the peak frequency of A_g-kd curve. This deviation is primarily attributed to insufficient spatial resolution within the narrow gap between structures, which compromises accuracy around resonance. As illustrated in Fig. 13, Fig. 14, Fig. 15, the simulation using a finer grid resolution $\delta x = B_g/40$ yields results that closely align with the NS-based benchmark in Ref [2]. To quantify this improvement, relative errors around the resonant frequency (kd =1.5 and 1.6) are presented in Table 7, calculated as $E_r = |\varphi_{\text{LBM}} - \varphi_{\text{NS}}|/\varphi_{\text{NS}}$, where φ_{LBM} and φ_{NS} represent the physical quantities from the present LBM and NS-based models, respectively. These results clearly demonstrate that grid refinement substantially enhances the predictive capability of the LBM

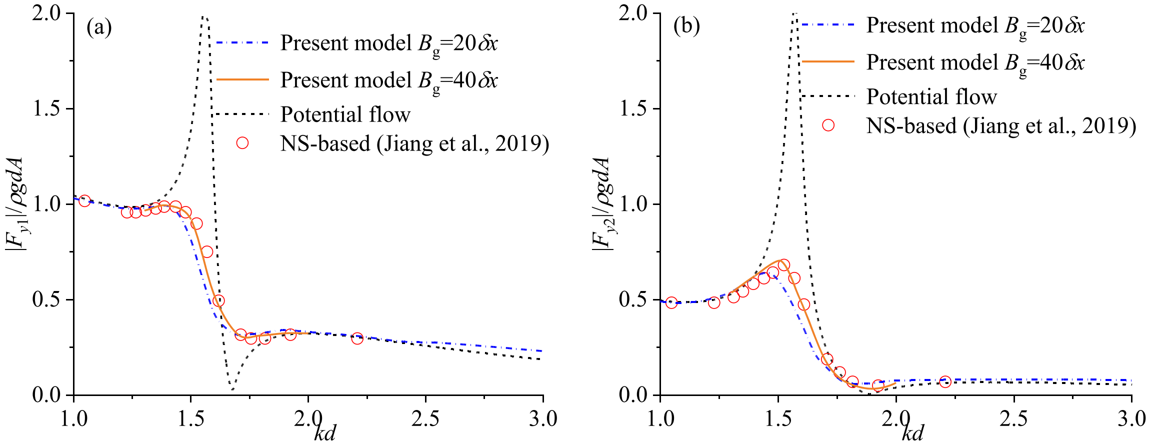

Fig. 15. Comparison of vertical forces on Box 1 and Box 2 versus dimensionless wavenumber obtained from the present model, NS-based model by Jiang et al [2]: (a) $|F_{y1}|/\rho gdA$ and (b) $|F_{y2}|/\rho gdA$.

Table 7
The relative errors E_r of the water surface elevation inside the gap and hydrodynamic forces acted on the two boxes for kd =1.5 and 1.6.

kd	δx	E_r				
		A_g	F_{x1}	F_{x2}	F_{y1}	F_{y2}
1.5	$B_g/20$	0.025	0.172	0.018	0.132	0.092
	$B_g/40$	0.073	0.100	0.049	0.012	0.059
1.6	$B_g/20$	0.156	0.051	0.159	0.262	0.251
	$B_g/40$	0.049	0.019	0.040	0.088	0.038

model in resolving resonance dynamics.

Nonetheless, due to the current implementation of uniform Cartesian grids without local mesh refinement strategies, the computational cost increases roughly as $O(N^3)$ with grid refinement in 2D framework, where N denotes the refinement factor. For the refined case of $\delta x = B_g/40$, the total number of computational cells reaches approximately 10 million even for a two-dimensional simulation, posing a significant computational burden. To balance accuracy and efficiency, a coarser resolution is adopted in most simulations, wherein 20 grid points are used to span the 0.05 m-wide gap region. In future work, the incorporation of local mesh refinement techniques may be explored to better handle the multi-scale nature of the problem, where large-scale wave propagation coexists with small-scale flow features such as those in narrow gaps.

Overall, the comparison results validate the robustness of the proposed LBM framework for simulating free surface flows involving partially submerged stationary structures, demonstrating its potential as an effective tool for hydrodynamic analysis in such configurations.

4. Concluding remarks

In this study, we developed a numerical model based on the MRT-LBM for simulating the partially submerged stationary structures in free surface flows. For high computational efficiency and stability, the LBM-characteristic VOF and the improved momentum exchange method were adopted to capture gas-liquid interface and evaluating hydrodynamic forces, respectively. Three benchmark cases were first performed for code verification: the flows over the circular and square cylinders, and Rider-Kothe single vortex evolution. Subsequently, two real-world problems, the dam-break flow and wave flow past two stationary boxes were simulated to validate the feasibility of coupling treatments for fluid-structure boundary and VOF methods. Compared with experimental and NS-based numerical results, it was confirmed that the developed LBM model is capable of simulating free surface deformation and accurately predicting the hydrodynamic forces for stationary bodies. These findings highlight the potential of LBM for extending its application to ocean engineering, where wave-structure interactions are of significant research interest.

CRediT authorship contribution statement

Baoming Guo: Writing – review & editing, Writing – original draft, Visualization, Validation, Methodology, Formal analysis, Conceptualization. **Jianping Meng:** Writing – review & editing, Supervision, Resources. **Zhihua Xie:** Writing – review & editing, Visualization, Validation. **Dezhi Ning:** Supervision. **Shunqi Pan:** Writing – review & editing, Supervision, Formal analysis.

Declaration of competing interest

The authors declare that they have no known competing financial interests or personal relationships that could have appeared to influence the work reported in this paper.

Acknowledgements

Support from the UK Engineering and Physical Sciences Research Council under the project “UK Consortium on Mesoscale Engineering Sciences (UKCOMES)” (Grant No. EP/X035875/1) is gratefully acknowledged. This work made use of computational support by CoSeC, the Computational Science Centre for Research Communities, through UKCOMES. This work has also been supported by Cardiff University Scholarship and China Scholarship Council (202006060048).

Appendix A. Boundary value problem

Based on linear potential flow theory, Fig. A1 shows a boundary value problem, and its governing equation and boundary conditions of those velocity potentials can be expressed as,

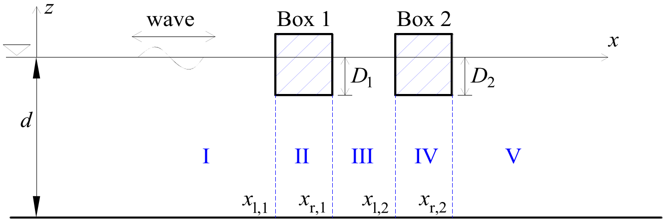

Fig. A1. The sketch of two stationary boxes.

$$\nabla^2\phi_n = \frac{\partial^2\phi_n}{\partial x} + \frac{\partial^2\phi_n}{\partial z^2} = 0 \tag{A.1}$$

$$\begin{cases} \dfrac{\partial\phi_n}{\partial z} = \dfrac{\omega^2}{g}\phi_n + \begin{cases} \dfrac{\mathrm{i}\omega}{\rho g}\delta_{n,1}, & x_{\mathrm{r},i} \le x \le x_{\mathrm{l},i+1},\ z=0 \\ 0, & x \le x_{\mathrm{l},1}, x \ge x_{\mathrm{r},2},\ z=0 \end{cases} \\ \dfrac{\partial\phi_n}{\partial x} = 0\ x = \ x_{\mathrm{l},i}, x = x_{\mathrm{r},i},\ -D_i \le z \le 0 \\ \dfrac{\partial\phi_n}{\partial z} = 0 \quad z = -d \\ \dfrac{\partial\phi_n}{\partial z} = 0\ x_{\mathrm{l},i} \le x \le x_{\mathrm{r},i},\ z = -D_i \\ \lim\limits_{x\to\pm\infty}\left\{\dfrac{\partial}{\partial x} \mp \mathrm{i}k\right\}(\phi_0 - \phi_{\mathrm{inc}}, \phi_1) = 0 \end{cases} \tag{A.2}$$

where, $\boldsymbol{x}_{r,i}$ and $\boldsymbol{x}_{l,i}$ are the x coordinates of right and left surface for the i^{th} box; $-D_i$ is y coordinate of the box bottom. The total potential is expressed as $\phi = \sum_{n=0}^{1}\zeta_n\phi_n$ in which ϕ_0 and ϕ_1 are the diffraction and radiation potentials. They can be expressed in each subdomain (I, II, III, IV, V) shown in Fig. A1 as,

$$\phi_n^{\mathrm{I}} = -\frac{\mathrm{i}gA}{\omega}\sum_{m=0}^{\infty} A_{n,m}^{\mathrm{I}} e^{\lambda_m x} Z_m(k_m z) + \phi_{\mathrm{inc}}\delta_{n,0} \tag{A.3}$$

$$\phi_n^{\mathrm{II}} = -\frac{\mathrm{i}gA}{\omega}\left[\left(A_{n,0}^{\mathrm{II}} + B_{n,0}^{\mathrm{II}}x\right)Y_0(\gamma_0 z) + \sum_{m=1}^{\infty}\left(A_{n,m}^{\mathrm{II}}e^{\gamma_m x} + B_{n,m}^{\mathrm{II}}e^{-\gamma_m x}\right)Y_m(\gamma_m z)\right] \tag{A.4}$$

$$\phi_n^{\mathrm{III}} = -\frac{\mathrm{i}gA}{\omega}\sum_{m=0}^{\infty}\left(A_{n,m}^{\mathrm{III}}e^{\lambda_m x} + B_{n,m}^{\mathrm{III}}e^{-\lambda_m x}\right)Z_m(k_m z) - \frac{\mathrm{i}}{\rho\omega}\delta_{n,1} \tag{A.5}$$

$$\phi_n^{\mathrm{IV}} = -\frac{\mathrm{i}gA}{\omega}\left[\left(A_{n,0}^{\mathrm{IV}} + B_{n,0}^{\mathrm{IV}}x\right)Y_0(\gamma_0 z) + \sum_{m=1}^{\infty}\left(A_{n,m}^{\mathrm{IV}}e^{\gamma_m x} + B_{n,m}^{\mathrm{IV}}e^{-\gamma_m x}\right)Y_m(\gamma_m z)\right] \tag{A.6}$$

$$\phi_n^{\mathrm{V}} = -\frac{\mathrm{i}gA}{\omega}\sum_{m=0}^{\infty} A_{n,m}^{\mathrm{V}} e^{-\lambda_m x} Z_m(k_m z) \tag{A.7}$$

where k_m and γ_m are eigenvalues, and $Z_m(k_m z)$ and $Y_m(\gamma_m z)$ are vertical eigenfunctions at given subdomains,

$$Z_m = \begin{cases} \dfrac{\cosh k_0(z+d)}{\sqrt{N_0}} \\ \dfrac{\cos k_m(z+d)}{\sqrt{N_m}} \end{cases} \text{with } N_m = \begin{cases} \dfrac{1}{2}\left(1 + \dfrac{\sinh 2k_0 d}{2k_0 d}\right),\ j=0 \\ \dfrac{1}{2}\left(1 + \dfrac{\sin 2k_m d}{2k_m d}\right),\ j \ge 1 \end{cases}$$

$$Y_m = \begin{cases} \dfrac{\sqrt{2}}{2},\ j=0 \\ \cos\gamma_m(z+d),\ j \ge 1 \end{cases}$$

The continuous pressure and velocity need to be satisfied between the adjacent subdomains. At the right and left boundaries of the first box, it has,

$$\frac{\partial \phi_m^{\mathrm{I}}}{\partial x} = \begin{cases} \frac{\partial \phi_m^{\mathrm{II}}}{\partial x} \ x = \ x_{\mathrm{l},1}, -d \le z \le -D_1 \\ 0, \ x = \ x_{\mathrm{l},1}, -D_1 \le z \le 0 \end{cases} \tag{A.8}$$

$$\frac{\partial \phi_m^{\mathrm{III}}}{\partial x} = \begin{cases} \frac{\partial \phi_m^{\mathrm{II}}}{\partial x} \ x = \ x_{\mathrm{r},1}, -d \le z \le -D_1 \\ 0, \ x = \ x_{\mathrm{r},1}, -D_1 \le z \le 0 \end{cases} \tag{A.9}$$

$$\phi_m^{\mathrm{I}} = \phi_m^{\mathrm{II}}, \ x = \ x_{\mathrm{l},1}, -d \le z \le -D_1 \tag{A.10}$$

$$\phi_m^{\mathrm{III}} = \phi_m^{\mathrm{II}}, \ x = \ x_{\mathrm{r},1}, -d \le z \le -D_1 \tag{A.11}$$

Similar continuous conditions exist at the boundaries of the second ones. Then a set of linear algebraic equations can be deduced to determine those unknown coefficients by substituting Eqs. A.3 – A.7 into continuous conditions and applying the orthogonality of vertical eigenfunctions. It should be mentioned the radiation potential denotes the hydrodynamic response when the free surface between two boxes (subdomain III) is imposed the external air pressure. More details regarding the theoretical model can be found in [69,70].

Data availability

I have shared the link to my code at the Attached File Step.

References

[1] F. Opoku, M.N. Uddin, M. Atkinson, A review of computational methods for studying oscillating water columns – the Navier-Stokes based equation approach, Renew. Sustain. Energy Rev. 174 (2023).

[2] S.-C. Jiang, W. Bai, P.-W. Cong, B. Yan, Numerical investigation of wave forces on two side-by-side non-identical boxes in close proximity under wave actions, Mar. Struct. 63 (2019) 16–44.

[3] L. Lu, B. Teng, L. Sun, B. Chen, Modelling of multi-bodies in close proximity under water waves—fluid forces on floating bodies, Ocean Eng. 38 (2011) 1403–1416.

[4] J. Yan, A. Korobenko, X. Deng, Y. Bazilevs, Computational free-surface fluid-structure interaction with application to floating offshore wind turbines, Comput. Fluids 141 (2016) 155–174.

[5] W.J. Cao, Z. Li, X.H. Li, D.Le Touzé, A regularized single-phase lattice Boltzmann method for free-surface flows, Comput. Math. Appl. 80 (2020) 2194–2211.

[6] T. Krüger, H. Kusumaatmaja, A. Kuzmin, O. Shardt, G. Silva, E.M. Viggen, The Lattice Boltzmann Method, Springer, Cham, 2017.

[7] G. Liu, J. Zhang, Q. Zhang, A high-performance three-dimensional lattice Boltzmann solver for water waves with free surface capturing, Coast. Eng. (2021) 165.

[8] C. Schwarzmeier, M. Holzer, T. Mitchell, M. Lehmann, F. Häusl, U. Rüde, Comparison of free-surface and conservative Allen-Cahn phase-field lattice Boltzmann method, J. Comput. Phys. (2023) 473.

[9] H.E. Morrison, A. Leder, Sediment transport in turbulent flows with the lattice Boltzmann method, Comput. Fluids 172 (2018) 340–351.

[10] C. Peng, Y. Teng, B. Hwang, Z. Guo, L.-P. Wang, Implementation issues and benchmarking of lattice Boltzmann method for moving rigid particle simulations in a viscous flow, Comput. Math. Appl. 72 (2016) 349–374.

[11] C. Peng, O.M. Ayala, L.-P. Wang, A comparative study of immersed boundary method and interpolated bounce-back scheme for no-slip boundary treatment in the lattice Boltzmann method: Part I, laminar flows, Comput. Fluids 192 (2019).

[12] A.K. Gunstensen, D.H. Rothman, S. Zaleski, G. Zanetti, Lattice Boltzmann model of immiscible fluids, Phys. Rev. A 43 (1991) 4320–4327.

[13] M.R. Swift, W.R. Osborn, J.M. Yeomans, Lattice Boltzmann simulation of nonideal fluids, Phys. Rev. Lett. 75 (1995) 830–833.

[14] X. Shan, H. Chen, Lattice Boltzmann model for simulating flows with multiple phases and components, Phys. Rev. Stat. Phys. Plasmas. Fluids Relat. Interdiscip. Top. 47 (1993) 1815–1819.

[15] C. Korner, M. Thies, T. Hofmann, N. Thurey, U. Rude, Lattice Boltzmann model for free surface flow for modeling foaming, J. Stat. Phys. 121 (2005) 179–196.

[16] G. Thömmes, J. Becker, M. Junk, A.K. Vaikuntam, D. Kehrwald, A. Klar, et al., A lattice Boltzmann method for immiscible multiphase flow simulations using the level set method, J. Comput. Phys. 228 (2009) 1139–1156.

[17] Y. Yu, L. Chen, J.H. Lu, G.X. Hou, A coupled lattice Boltzmann and particle level set method for free-surface flows, Scienceasia 40 (2014) 238–247.

[18] C. Janssen, M. Krafczyk, A lattice Boltzmann approach for free-surface-flow simulations on non-uniform block-structured grids, Comput. Math. Appl. 59 (2010) 2215–2235.

[19] C. Janssen, M. Krafczyk, Free surface flow simulations on GPGPUs using the LBM, Comput. Math. Appl. 61 (2011) 3549–3563.

[20] Y. Thorimbert, J. Latt, L. Cappietti, B. Chopard, Virtual wave flume and Oscillating Water Column modeled by lattice Boltzmann method and comparison with experimental data, Int. J. Mar. Energy 14 (2016) 41–51.

[21] G.-w. Liu, Q.-h. Zhang, J.-f. Zhang, Development of two-dimensional numerical wave tank based on lattice Boltzmann method, J. Hydrodyn. 32 (2019) 116–125.

[22] G. Liu, Q. Zhang, J. Zhang, Numerical wave simulation using a modified lattice Boltzmann scheme, Comput. Fluids 184 (2019) 153–164.

[23] L.C. Qiu, L. Tian, X.J. Liu, Y. Han, A 3D multiple-relaxation-time LBM for modeling landslide-induced tsunami waves, Eng. Anal. Bound. Elem. 102 (2019) 51–59.

[24] L. Chen, Y. Yu, J.H. Lu, G.X. Hou, A comparative study of lattice Boltzmann methods using bounce-back schemes and immersed boundary ones for flow acoustic problems, Int. J. Numer. Methods Fluids 74 (2014) 439–467.

[25] H. Li, X. Lu, H. Fang, Y. Qian, Force evaluations in lattice Boltzmann simulations with moving boundaries in two dimensions, Phys. Rev. E Stat. Nonlin. Soft Matter. Phys. 70 (2004) 026701.

[26] Y. Chen, Q. Cai, Z. Xia, M. Wang, S. Chen, Momentum-exchange method in lattice Boltzmann simulations of particle-fluid interactions, Phys Rev Stat Nonlin Soft Matter Phys 88 (2013) 013303.

[27] B. Wen, C. Zhang, Y. Tu, C. Wang, H. Fang, Galilean invariant fluid–solid interfacial dynamics in lattice Boltzmann simulations, J. Comput. Phys. 266 (2014) 161–170.

[28] Z. Li, G. Oger, D.Le Touzé, A partitioned framework for coupling LBM and FEM through an implicit IBM allowing non-conforming time-steps: application to fluid-structure interaction in biomechanics, J. Comput. Phys. (2022) 449.

[29] J.C.B. de Motta, P. Costa, J.J. Derksen, C. Peng, L.P. Wang, W.P. Breugem, et al., Assessment of numerical methods for fully resolved simulations of particle-laden turbulent flows, Comput. Fluids 179 (2019) 1–14.

[30] C. Peng, O.M. Ayala, J.C.B. de Motta, L.P. Wang, A comparative study of immersed boundary method and interpolated bounce-back scheme for no-slip boundary treatment in the lattice Boltzmann method: Part II, turbulent flows, Comput. Fluids 192 (2019).

[31] T. Fringand, I. Cheylan, M. Lenoir, L. Mace, J. Favier, A stable and explicit fluid-structure interaction solver based on lattice-Boltzmann and immersed boundary methods, Comput. Methods Appl. Mech. Eng. (2024) 421.

[32] Z.M. Zhao, P. Huang, Y.N. Li, J.M. Li, A lattice Boltzmann method for viscous free surface waves in two dimensions, Int. J. Numer. Methods Fluids 71 (2013) 223–248.

[33] S. Watanabe, J. Kawahara, T. Aoki, K. Sugihara, S. Takase, S. Moriguchi, et al., Free-surface flow simulations with floating objects using lattice Boltzmann method, Eng. Appl. Comput. Fluid Mech. 17 (2023).

[34] J.H. Zhou, G.W. Liu, Q.H. Zhang, J.F. Zhang, Development and application of a numerical wave tank using the phase-field lattice Boltzmann method, Phys. Fluids 37 (2025).

[35] A.J.C. Ladd, Numerical Simulations of Particulate Suspensions Via a Discretized Boltzmann-Equation 1. Theoretical Foundation, J. Fluid Mech. 271 (1994) 285–309.

[36] K. Sato, K. Kawasaki, S. Koshimura, A comparative study of the cumulant lattice Boltzmann method in a single-phase free-surface model of violent flows, Comput. Fluids (2022) 236.

[37] H. Yuan, Y.Y. Zou, W. Diao, Y.F. Mao, A coupled two-dimensional-three-dimensional hydrodynamic model for simulating flood wave evolution in reservoirs and riverbeds, Phys. Fluids 37 (2025).

[38] S. Bogner, U. Rüde, Simulation of floating bodies with the lattice Boltzmann method, Comput. Math. Appl. 65 (2013) 901–913.

[39] P.L. Bhatnagar, E.P. Gross, M. Krook, A model for collision processes in gases. I. Small amplitude processes in charged and neutral one-component systems, Phys. Rev. 94 (1954) 511–525.

[40] J. Meng, Y. Zhang, N.G. Hadjiconstantinou, G.A. Radtke, X. Shan, Lattice ellipsoidal statistical BGK model for thermal non-equilibrium flows, J. Fluid Mech. 718 (2013) 347–370.

[41] X. Shan, X.-F. Yuan, H. Chen, Kinetic theory representation of hydrodynamics: a way beyond the Navier–Stokes equation, J. Fluid Mech. (2006) 550.

[42] Z.L. Guo, C.G. Zheng, B.C. Shi, Discrete lattice effects on the forcing term in the lattice Boltzmann method, Phys. Rev. E (2002) 65.

[43] P. Lallemand, L.S. Luo, Theory of the lattice Boltzmann method: Dispersion, dissipation, isotropy, Galilean invariance, and stability, Phys. Rev. E 61 (2000) 6546–6562.

[44] R. Mei, L.-S. Luo, P. Lallemand, D. d'Humières, Consistent initial conditions for lattice Boltzmann simulations, Comput. Fluids 35 (2006) 855–862.
[45] R. Scardovelli, S. Zaleski, Analytical Relations Connecting Linear Interfaces and Volume Fractions in Rectangular Grids, J. Comput. Phys. 164 (2000) 228–237.
[46] D. Yu, R. Mei, L.-S. Luo, W. Shyy, Viscous flow computations with the method of lattice Boltzmann equation, Prog. Aerosp. Sci. 39 (2003) 329–367.
[47] J. Choi, S.B. Yoon, Numerical simulations using momentum source wave-maker applied to RANS equation model, Coast. Eng. 56 (2009) 1043–1060.
[48] https://github.com/inmeso/hilemms.
[49] https://ops-dsl.readthedocs.io/en/latest/introduction.html.
[50] Y. Peng, H.C. Du, B. Wang, A curved boundary treatment for discrete Boltzmann model of shallow water flows based on a partially saturated method, J. Hydraul. Res. 61 (2023) 346–355.
[51] C. Tsigginos, J.P. Meng, X.J. Gu, D.R. Emerson, Lattice Boltzmann modeling of fluid-particle interaction based on a two-phase mixture representation, Phys. Rev. E 100 (2019).
[52] C. Tsigginos, J.P. Meng, X.J. Gu, D.R. Emerson, Coupled LBM-DEM simulations using the partially saturated method: Theoretical and computational aspects, Powder Technol. (2022) 405.
[53] D.J. Tritton, Experiments on the flow past a circular cylinder at low Reynolds numbers, J. Fluid Mech. 6 (2006) 547–567.
[54] C. Liu, X. Sheng, C.H. Sung, Preconditioned multigrid methods for unsteady incompressible flows, J. Comput. Phys. 139 (1998) 35–57.
[55] K. Taira, T. Colonius, The immersed boundary method: a projection approach, J. Comput. Phys. 225 (2007) 2118–2137.
[56] P.A. Berthelsen, O.M. Faltinsen, A local directional ghost cell approach for incompressible viscous flow problems with irregular boundaries, J. Comput. Phys. 227 (2008) 4354–4397.
[57] P.H. Chiu, R.K. Lin, T.W.H. Sheu, A differentially interpolated direct forcing immersed boundary method for predicting incompressible Navier–Stokes equations in time-varying complex geometries, J. Comput. Phys. 229 (2010) 4476–4500.
[58] M.N. Linnick, H.F. Fasel, A high-order immersed interface method for simulating unsteady incompressible flows on irregular domains, J. Comput. Phys. 204 (2005) 157–192.
[59] Z. Xie, An implicit Cartesian cut-cell method for incompressible viscous flows with complex geometries, Comput. Methods Appl. Mech. Eng. (2022) 399.
[60] A.K. Dhiman, R.P. Chhabra, A. Sharma, V. Eswaran, Effects of reynolds and prandtl numbers on heat transfer across a square cylinder in the steady flow regime, Numer. Heat Transf. A: Appl. 49 (2006) 717–731.
[61] A. Sohankar, C. Norberg, L. Davidson, Low-Reynolds-number flow around a square cylinder at incidence: study of blockage, onset of vortex shedding and outlet boundary condition, Int. J. Numer. Methods Fluids 26 (1998) 39–56.
[62] A. Sharma, V. Eswaran, Heat and fluid flow across a square cylinder in the two-dimensional laminar flow regime, Numer. Heat Transf. A: Appl. 45 (2004) 247–269.
[63] S. Sen, S. Mittal, G. Biswas, Flow past a square cylinder at low Reynolds numbers, Int. J. Numer. Methods Fluids 67 (2010) 1160–1174.
[64] W.J. Rider, D.B. Kothe, Reconstructing volume tracking, J. Comput. Phys. 141 (1998) 112–152.
[65] J.C. Martin, W.J. Moyce, Part IV. An experimental study of the collapse of liquid columns on a rigid horizontal plane, R. Soc. Lond. Philos. Trans. A 244 (1952) 312–324.
[66] W. Zhao, J. Liang, M. Sun, Z. Wang, Investigation on the effect of convective outflow boundary condition on the bubbles growth, rising and breakup dynamics of nucleate boiling, Int. J. Therm. Sci. 167 (2021).
[67] D.J.E. Harvie, D.F. Fletcher, A new volume of fluid advection algorithm: The Stream scheme, J. Comput. Phys. 162 (2000) 1–32.
[68] D.M. Greaves, Simulation of viscous water column collapse using adapting hierarchical grids, Int. J. Numer. Methods Fluids (2006) 693–711.
[69] B.M. Guo, D.Z. Ning, R.Q. Wang, B.Y. Ding, Hydrodynamics of an oscillating water column WEC - Breakwater integrated system with a pitching front-wall, Renew. Energy 176 (2021) 67–80.
[70] S. Zheng, A. Antonini, Y. Zhang, J. Miles, D. Greaves, G. Zhu, et al., Hydrodynamic performance of a multi-Oscillating Water Column (OWC) platform, Appl. Ocean Res. (2020) 99.